HySA/Catalysis Centre of Competence, Catalysis Institute

Department of Chemical Engineering

University of Cape Town


# Iridium Oxide Supported on Antimony-Doped Tin Oxide as an Electrocatalyst for the Oxygen Evolution Reaction

University of Cape Town

Submitted in partial fulfilment of the requirements for the degree of Master of Science in Chemical Engineering

**Author: Ziba Shabir Hussein Somjee Rajan**

**Supervisors: Dr. Rhiyaad Mohamed and Dr. Tobias Binninger**

February 2020

The copyright of this thesis vests in the author. No quotation from it or information derived from it is to be published without full acknowledgement of the source. The thesis is to be used for private study or non-commercial research purposes only.

Published by the University of Cape Town (UCT) in terms of the non-exclusive license granted to UCT by the author.

University of Cape Town

*"If passion drives you, let reason hold the reins."*

**Benjamin Franklin**

*For Sara.*

# PLAGIARISM DECLARATION

I know the meaning of plagiarism and declare that all the work in the document, save for that which is properly acknowledged, is my own. This thesis/dissertation has been submitted to the Turnitin module (or equivalent similarity and originality checking software) and I confirm that my supervisors have seen my report and any concerns revealed by such have been resolved with my supervisors.

**Name:** Ziba Shabir Hussein Somjee Rajan

**Date:** 10th February 2020

**Signature:** Signed by candidate

# ACKNOWLEDGMENTS

It is strange to think of how much my life has changed since joining HySA/Catalysis as Dr. Rhiyaad Mohamed's research assistant in December 2017. Here we are in January 2020, and I have presented an oral presentation at the *70th Annual Meeting of the International Society of Electrochemistry*, and we have submitted some of this work for publication. While these achievements are partly as a result of my passion and commitment towards this work, these achievements are also a true testament to the supervision of Rhiyaad Mohamed and Tobias Binninger.

Rhiyaad Mohamed – where to begin. Thank you for choosing me to be the first student of your academic career. Thank you for exposing me to so many incredible opportunities and for standing in the lab with me whenever I have needed help. Thank you for the rigorous training in electrochemical characterisation techniques and for teaching me how to become an independent electrochemist. You have always had a lot of faith in my abilities, most times more than I had in myself. The advice you have given me as a mentor has really shaped my character and given me confidence as a researcher. I really appreciate you giving me a chance to engage in work that was beyond the scope of my thesis, for this work has made me a more critical and engaged researcher. I am truly passionate about the research that we do, and the exposure you have given me has only honed and refined my understanding and expertise in this exciting research field.

To Tobias Binninger, thank you for teaching me that in science, there is nothing more important than integrity. You have taught me how to reason, to think, and to question. Thank you for always supporting me, for asking the tough questions, for always believing in this work, and for listening to my ideas. You have really taught me a lot and I will carry all these learnings throughout my career. Thank you for being so involved in the project despite being all the way on the other side of the world. I really appreciate all the evenings which you made available for those 3-4 hour skype calls, where we would make all the major decisions about the direction of the work.

Darija Susac, thank you for being a great mentor and teacher to me. Your contribution to the work with X-ray photoelectron spectroscopy (XPS) has been invaluable. Thank you for taking the time to talk me through every part of the XPS analysis and interpretation in such a way that I could actually understand it. Most of all, thank you for your guidance with the writing of our publication; this was the most challenging task I have ever had to do and I couldn't have done it without your unwavering support and guidance.

To Richard Martin and Patricia Kooyman, thank you for taking all the high-resolution transmission electron microscopy images and energy dispersive X-ray spectroscopy maps that were used in this work; I especially appreciate you both making the trips to Nelson Mandela Metropolitan University in Port Elizabeth to take these measurements.

I acknowledge Brian Doyle and Emanuella Carleschi for taking all the X-ray photoelectron spectroscopy measurements at the University of Johannesburg, for the purpose of this thesis. I also acknowledge the electron microscopy unit at the University of Cape Town, in particular Nasheeta Hanief and Miranda Waldron, for their assistance with energy dispersive X-ray spectroscopy measurements.

This work is based on the research supported in part by the National Research Foundation of South Africa Grant numbers 94878 and 93205. I acknowledge the Dutkiewicz Family Scholarship for postgraduate research in energy, as well as the HySA/Catalysis Centre of Competence DST for funding my Master's degree.

A special thank you to Julie-Ann Hoffman, Firdaus Hendricks, Loren de Koker, Richard Martin, Michaelan Sinnett, my sister Sara and my parents, for constantly supporting me during the many tough times in the course of these past two years. I couldn't have done any of this without you.

# CONFERENCE CONTRIBUTIONS

## 2019

Z. Rajan, T. Binninger, and R. Mohamed

*"IrOx Supported on Antimony-Doped Tin Oxide as a High-Performing Electrocatalyst for the Oxygen Evolution Reaction"*

Oral presentation at the 70th Annual Meeting of the International Society of Electrochemistry, Durban, South Africa.

## 2018

Z. Rajan, T. Binninger, and R. Mohamed

*"IrOx on Sb-doped Tin Oxide (ATO) for the Oxygen Evolution Reaction (OER)"*

Oral presentation at the 29th Annual Meeting of the Catalysis Society of South Africa, Limpopo, South Africa.

Z. Rajan, T. Binninger, and R. Mohamed

*"IrOx on Sb-doped Tin Oxide (ATO) for the Oxygen Evolution Reaction (OER)"*

Poster presentation at the 30th Steering Committee of the International Partnership for Hydrogen and Fuel Cells in the Economy, Pretoria, South Africa.

# ABSTRACT

The generation of high purity hydrogen by renewable, sustainable means is a crucial building block towards the realisation of a carbon-free energy economy. Proton exchange membrane water electrolysis (PEMWE) offers a promising route for the generation of clean hydrogen, using renewable energy, for both stationary and mobile energy storage applications, and as a feedstock for the chemical industry. As water electrolysis is an electrochemical redox reaction, cathodic hydrogen evolution cannot occur without an efficient, and rapid anodic oxygen evolution reaction (OER). While both iridium and ruthenium oxides are state-of-the-art OER catalysts in acidic environment, the latter undergoes dissolution under anodic OER conditions much more rapidly than the former, and this makes iridium oxide the most suitable catalytic material for electrolyser anodes. Several strategies have been explored as a means to lower the iridium content in OER catalysts, and of these, the use of cheap, stable support materials has been seen as a promising means to produce highly active, durable catalysts, by enhancement of the electrocatalytically active surface area.

In this thesis, the viability of an organometallic chemical deposition method for the deposition of $IrO_x$ nanoparticles on antimony-doped tin oxide (ATO) support is investigated. The effect of the gas environment (oxygen or argon) and the temperature used for the deposition was examined. The *ex-situ* OER performance of the synthesised electrocatalysts was evaluated using the rotating disk electrode technique. Using X-ray photoelectron spectroscopy (XPS) and high-resolution transmission scanning electron microscopy (HR-STEM), the physical properties of the synthesised $IrO_x$/ATO catalysts were elucidated, in order to understand the observed oxygen evolution activity and stability of $IrO_x$/ATO in relation to the OMCD technique. In addition to developing an understanding towards the physical and electrochemical properties of the synthesised materials, strategies to optimise the Ir yield achieved by the organometallic chemical deposition process were explored.

# TABLE OF CONTENTS

# LIST OF FIGURES

## Chapter 2



## Chapter 4



## Chapter 5



## Chapter 6

## Chapter 8



## Appendix A



## Appendix B

# LIST OF TABLES

## Chapter 2



## Chapter 4



## Chapter 5



## Chapter 6



## Chapter 8



## Appendix C

# NOMENCLATURE

**List of Abbreviations**

| | |
|---|---|
| PEMWE | Proton exchange membrane electrolysis |
| OER | Oxygen evolution reaction |
| ATO | Antimony-doped tin oxide |
| OMCVD | Organometallic chemical vapor deposition |
| OMCD | Organometallic chemical deposition |
| XRD | X-ray diffraction |
| XPS | X-Ray photoelectron spectroscopy |
| ICP-OES | Inductively coupled plasma – optical emission spectroscopy |
| EDX | Energy dispersive x-ray |
| HR-STEM | High-resolution transmission electron microscopy |
| HAADF | High angle annular dark field |
| SEM | Scanning electron microscopy |
| RHE | Reversible hydrogen electrode |
| RDE | Rotating disk electrode |
| CV | Cyclic voltammetry |
| CA | Chronoamperometry |
| EIS | Electrochemical impedance spectroscopy |

# Chapter 1: Introduction

*The purpose of this thesis is to explore organometallic chemical deposition as a method to synthesise iridium oxides on antimony-doped tin oxide support, as catalysts for the oxygen evolution reaction in proton exchange membrane water electrolysis. This chapter summarises the overall aim and scope of this project.*

The generation of high purity hydrogen by renewable, sustainable means is a crucial building block towards the realisation of a carbon-free energy economy. Proton exchange membrane water electrolysis (PEMWE) offers a promising route for the generation of clean hydrogen, using renewable energy, for both stationary and mobile energy storage applications and as a feedstock for the chemical industry. As water electrolysis is an electrochemical redox reaction, cathodic hydrogen evolution cannot occur without an efficient and rapid anodic oxygen evolution reaction (OER). While both iridium and ruthenium oxides are state-of-the-art OER catalysts in acidic environment, the latter undergoes dissolution under anodic OER conditions much more rapidly than the former, and this makes iridium oxide the most suitable catalytic material for PEMWE anodes (Reier, Oezaslan & Strasser, 2012).

For electrolyser technology to reach widespread commercialisation, it is critical that the iridium loading in anode catalysts is reduced to a point where the performance of these catalysts greatly outweighs their cost. Various approaches have been explored to lower iridium content while maintaining high OER performance: iridium-iridium oxide core-shell concepts (Nong et al., 2014; Kim et al., 2017), bimetallic oxides (Owe et al., 2012; Audichon et al., 2014), high-surface area amorphous iridium oxides (Smith et al., 2014; Abbott et al., 2016), and the use of iridium oxide nanoparticles supported on inexpensive materials (Marshall & Haverkamp, 2010; Fuentes, Farell & Weidner, 2011; Puthiyapura et al., 2014; Hu, Chen & Xia, 2014; Liu et al., 2015; Oh et al., 2015, 2016; Tong et al., 2017; Massué et al., 2017; Böhm et al., 2019; Solà-Hernández et al., 2019; Lebedev & Copéret, 2019; Ohno et al., 2019) to enhance iridium utilisation by maximising the electrocatalytically active area.

For the latter approach, the support materials need to exhibit high surface area and be electronically conductive as well as low cost materials, which are capable of forming porous structures that are stable in highly acidic and oxidising environments. These are challenging criteria to meet, and while carbon has played a starring role as an electrocatalytic support material in fuel cell applications, it is unsuitable for anodic electrolyser applications as a result of carbon corrosion which is prominent at the high oxidative potentials ($E > 1.5$ V vs. RHE) of the oxygen evolution reaction(Maillard, Bonnefont & Micoud, 2011; Rozain et al., 2016).

Sasaki et al.(Sasaki et al., 2010) evaluated the thermodynamic stability of various metal oxides as alternative support materials to carbon black, under severe operating conditions for PEM fuel cell applications; thermodynamic calculations showed that $SnO_2$ and $TiO_2$ are feasible, oxidation-resistant support materials, particularly in instances where the operating potential exceeds 1.4 V vs. RHE. While this is a strong motivation for the use of such materials as electrolyser supports, these oxides offer little electronic conductivity. Doping with metal cations or anions such as fluoride can create electronic defects in these materials, and subsequently create the desired electronic conductivity (Nütz, Zum Felde & Haase, 1999; Zhang & Gao, 2004; Elangovan & Ramamurthi, 2005). Over the past five years, antimony-doped tin oxide (ATO) has gained significant attention as an anodic catalyst support material for Ir-based catalysts in OER applications. In some of these works, $IrO_x$ nanoparticles were deposited onto ATO support by means of Adams' fusion (Puthiyapura et al., 2014; Liu et al., 2015), a colloidal method (Tong et al., 2017), a chemical reduction method to deposit $IrO_x$ nanoparticles on ATO aerogel (Solà-Hernández et al., 2019), and most recently a solvothermal technique for the deposition of $IrO_x$ on macroporous ATO support. In other studies, metallic Ir nanodendrites (ND) or nanoparticles (NP) were deposited on ATO support by means of chemical reduction (Oh et al., 2015), the polyol method (Oh et al., 2016), and microwave-assisted hydrothermal deposition (Massué et al., 2017).

Organometallic chemical deposition (OMCD) is a technique which has been proven to be highly effective for the deposition of Pt nanoparticles on carbon, carbide, and oxide support materials for fuel cell electrocatalysis (Taylor et al., 2016; Jackson, Conrad & Levecque, 2017; Mohamed et al., 2018). These studies used the decomposition of platinum acetylacetonate to deposit well-dispersed platinum nanoparticles onto various support materials by optimisation of the gas environment and temperature used for the deposition process. This is a one-step method that offers simplicity in comparison to wet chemistry techniques which require numerous process and post-treatment steps.

In the present work, we investigate the viability of the OMCD method for the deposition of iridium oxide nanoparticles on ATO support. The *ex-situ* OER performance of this electrocatalyst was evaluated using the rotating disk electrode technique. Using X-ray photoelectron spectroscopy (XPS) and high resolution transmission scanning electron microscopy (HR-STEM), we studied the structural and chemical characteristics of the iridium oxide in order to understand the observed oxygen evolution activity and stability of $IrO_x$/ATO in relation to the OMCD technique.

# Chapter 2: Literature Review

*This chapter describes the critical role of proton exchange membrane water electrolysis in a hydrogen-based energy economy, and outlines the challenges which are associated with the realization of this technology. The need for efficient, cost-effective, iridium-based catalytic materials for the oxygen evolution reaction is exemplified. A systematic motivation for the use of oxide-supported iridium oxide catalysts is provided, and the various methods which exist for the synthesis of such materials are discussed. Finally, organometallic chemical deposition is discussed as a promising method to be explored for the synthesis of iridium oxide, supported on antimony-doped tin oxide.*

## 2.1 THE HYDROGEN ECONOMY

Hydrogen is an incredibly versatile molecule that is used as a feedstock to several industrial processes to produce ammonia, methanol and synthetic fuels, to name a few. Despite the vast potential for hydrogen, it is critical to note that most of its production processes originate from fossil fuel feedstocks, and thus there is almost always a high $CO_2$ footprint when synthesising hydrogen by these methods. As the effects of climate change become increasingly more severe, it has become incredibly important that the scientific community strives towards the production of hydrogen by more environmentally sustainable means.

As of 2008, 96 % of global hydrogen production came from the reforming, gasification and processing of natural gas, coal and oil; the 4 % balance in production resulted from water electrolysis pilot technology (Kothari, Buddhi & Sawhney, 2008). There are three types of water electrolysis that are currently in usage, these are: alkaline, proton exchange membrane (PEM) and solid oxide electrolysis technologies. ***Figure 2-1*** below shows these three electrolysis technologies, together with their anode and cathode equations. While alkaline electrolysis (AEL) is a mature, well-developed technology, the current densities achieved are low, and a corrosive (KOH) electrolyte is used, limiting the flexibility of its applications. On the other hand, solid oxide electrolysis is a high temperature electrolysis method which is useful in co-electrolysis processes, as well as for applications in chemical plants where heat integration is available. However, of these methods, PEM water electrolysis has been identified as the most viable method of hydrogen production over the other methods, on the basis of its compact system design, high current-densities, flexibility, versatility and pressurized operation (Buttler & Spliethoff, 2018; de Vasconcelos & Lavoie, 2019).

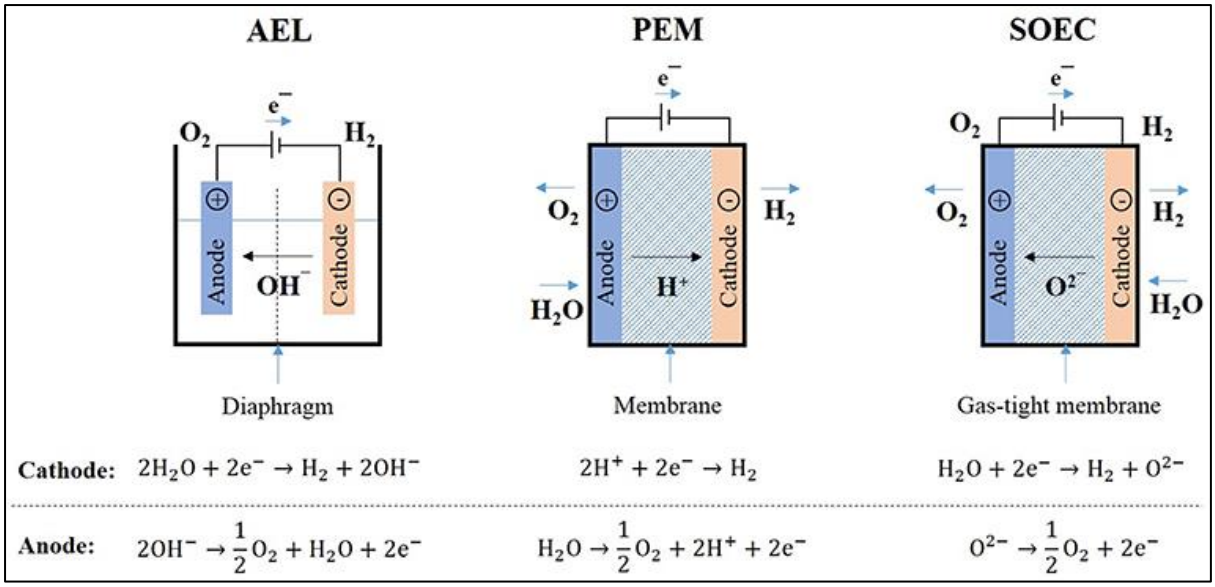


***Figure 2-1:****Technologies for alkaline (AEL), proton exchange membrane (PEM) and solid oxide electrolysis (SOEC), with anode and cathode half reactions, taken from de Vasconcelos & Lavoie (2019).*

## 2.2 PROTON EXCHANGE MEMBRANE WATER ELECTROLYSIS

PEM water electrolysers provide clean, high purity hydrogen with almost zero emissions (Sapountzi et al., 2017). While this is a highly attractive technology for hydrogen generation, rare and expensive noble metal catalysts are required for efficient and feasible operation. As seen in ***Figure 2-1*** above, two electrochemical reactions take place to convert water into hydrogen and oxygen - these are the hydrogen and oxygen evolution reactions.

The hydrogen evolution reaction is kinetically rapid and therefore only requires small loadings of platinum on carbon catalysts for feasible operation (Wei et al., 2019). However, the oxygen evolution reaction (OER), which takes place at the anode of a PEM water electrolyser, has sluggish kinetics and thus requires the use of large quantities of catalyst to reach the required current-densities; the current state-of-the-art catalysts are unsupported oxides of iridium or ruthenium oxides. Iridium oxides offer both high activity and stability in electrolyser conditions, in contrast to the high activity and poor stability shown by ruthenium oxide, and this has resulted in iridium oxides being most common PEMWE anode catalysts (Reier, Oezaslan & Strasser, 2012).

## 2.3 FACTORS AFFECTING THE PERFORMANCE OF IRIDIUM-BASED OER CATALYSTS

The performance of any given OER catalyst can be understood as a function of its activity, durability and selectivity (Fabbri et al., 2014). Having said this, various physical, chemical and electronic properties of OER catalysts affect their performance. These properties, together with the reasons for their effects on OER performance have been summarised below.

#### *2.3.1.1 Particle Size and Spatial Dispersion*

Iridium oxides with particle sizes in the narrow range of 2-5 nm have been shown to exhibit the unique combination of high surface area (and high activity) and particle stability (Reier, Oezaslan & Strasser, 2012; Abbott et al., 2016); these oxides can degrade by agglomeration and therefore particles need to be large enough to withstand the need to agglomerate at high potentials for prolonged periods of time. In the context of supported catalysts, it is important to ensure that relatively small catalyst particles such as these have large enough inter-particle distances, so that the possibility of deactivation by particle agglomeration is minimised. To achieve high surface area, well-utilised supported catalysts, a high degree of spatial particle dispersion is required.

#### *2.3.1.2 Crystallinity and Iridium Oxidation State*

It is known that amorphous iridium oxide is much more active than rutile, crystalline $IrO_2$ towards the OER. While it has been speculated that the reason for this is as a result of the higher surface area present in amorphous $IrO_x$ than rutile $IrO_2$, the 16-fold increase in OER activity observed in the amorphous oxide cannot be explained by the effect of surface area alone. In the past few years many groups have pursued mechanistic studies into the OER on iridium oxide and it has been shown both thermodynamically and spectroscopically that the participation of oxygen species from iridium oxide structure plays a crucial role in the OER reaction mechanism. Binninger et al. (2015) illustrated using thermodynamic correlations the instability and therefore reactivity of the oxygen anion in transition metal oxides during the OER. Grimaud et al. (2017) used density functional theory (DFT) together with electrochemical characterisation to prove that the metal-oxygen valence in the bulk electronic structure of transition metal oxides governs the reaction mechanism and the activity in the OER; the activation of the lattice oxygen in these transition metal oxide catalysts can open and promote new reaction pathways in the OER.

Lastly, Pfeifer, Jones, Wrabetz, et al. (2016) explained that the central reason around the activity enhancement seen experimentally with amorphous as opposed to rutile iridium oxide, is in the fact that the amorphous structure offers mobility to the reactive oxygen species (whose importance to OER activity has been highlighted above); in the rutile structure the oxygen species are bonded to the maximum extent, preventing mobility of the reactive, electrophilic oxygen species, resulting in poor activity.

The oxidation state of iridium is tied very closely to the crystallinity of the iridium oxide phase. Rutile iridium oxide contains iridium which exists in the IV oxidation state only, where as it has been seen that amorphous iridium oxide can be classified as having an intermediate III/IV oxidation state (Pfeifer, Jones, Velasco Vélez, et al., 2016). Iridium metal can be active in the OER upon subjection to an oxidising electrochemical potential where it forms an amorphous iridium oxide (Kötz, 1984; Saveleva et al., 2018).

## 2.4 SUPPORTED IRIDIUM CATALYSTS

For PEM electrolyser technology to reach widespread commercialisation, it is critical that the iridium loading in anode catalysts is reduced to a point where the performance of these catalysts greatly outweighs their cost. Various approaches have been explored to lower iridium content while maintaining high OER performance: iridium-iridium oxide core-shell concepts (Nong et al., 2014; Kim et al., 2017), synthesis of bimetallic mixed oxides (Owe et al., 2012; Audichon et al., 2014), high-surface area amorphous iridium oxides (Smith et al., 2014; Abbott et al., 2016), and the use of iridium oxide nanoparticles supported on inexpensive materials (Marshall & Haverkamp, 2010; Fuentes, Farell & Weidner, 2011; Puthiyapura et al., 2014; Hu, Chen & Xia, 2014; Liu et al., 2015; Oh et al., 2015, 2016; Tong et al., 2017; Massué et al., 2017; Böhm et al., 2019; Solà-Hernández et al., 2019; Lebedev & Copéret, 2019; Ohno et al., 2019) to enhance iridium utilisation by maximising the electrocatalytically active surface area.

The criteria for OER support materials is a challenging one to meet. Schmidt (2012) explained the requirements for oxygen reduction reaction fuel cell support materials in extreme operating conditions (start-up/shutdown); these criteria are identical to those for oxygen evolution electrolyser applications. Therefore, the requirements for OER support materials are as follows (Sasaki et al., 2010; Schmidt, 2012):

1. Electronic conductivity – to allow for electrons to move to and from reactive interfaces and maximise catalyst utilisation
2. Structure giving – form porous catalyst layers to overcome internal mass transfer effects
3. Dissolution stability in highly acidic and oxidative environments – the leaching of metallic cations from support materials can exchange proton sites in the ionomer and membrane of an electrolyser, causing a rapid loss of performance
4. High surface area – for maximised catalyst utilisation and accessibility to the reaction interface
5. Low cost – the use of a support material is intended for enhanced utilisation of noble metal, to cause an overall cost reduction by a drastic decrease in noble metal content; it is therefore essential that the support material itself is significantly cheaper than the noble metal catalyst in question

While carbon has played a starring role as an electrocatalytic support material in fuel cell applications, it is unsuitable for anodic electrolyser applications as a result of carbon corrosion which is prominent at the high oxidative potentials ($E > 1.5$ V vs. the reversible hydrogen electrode) of the OER (Maillard, Bonnefont & Micoud, 2011; Rozain et al., 2016).

Sasaki et al. (2010) evaluated the thermodynamic stability of various metal oxides as alternative support materials to carbon black, under severe operating conditions for PEM fuel cell applications; thermodynamic calculations showed that $SnO_2$ and $TiO_2$ are feasible, oxidation-

resistant support materials, particularly in instances where the operating potential exceeds 1.4 V vs. RHE. While this is a strong motivation for the use of such materials as electrolyser supports, these oxides offer little electronic conductivity. Doping with metal cations or anions such as fluoride can create electronic defects in these materials, and subsequently create the desired electronic conductivity (Nütz, Zum Felde & Haase, 1999; Zhang & Gao, 2004; Elangovan & Ramamurthi, 2005). Over the past five years, antimony-doped tin oxide (ATO) has gained significant attention as an anodic catalyst support material in OER applications.

ATO-supported iridium oxides for OER applications have been greatly pursued over the past few years. In addition to the benefits of supported catalysts mentioned above, iridium oxides in these catalysts have also been shown to interact with the ATO in a manner which improves the overall catalyst activity and stability towards oxygen evolution. Oh et al. (2016) showed with *ex-situ* studies that while $IrO_x$ supported on carbon degraded rather rapidly, $IrO_x$ on ATO was stabilised during OER, seemingly by the ATO support. Massué et al. (2017) prepared metallic iridium nanoparticles on ATO, and here using temperature programmed reduction and XPS studies, it was seen that the oxidation state of iridium was present in a 3.3+ state, suggesting an interactive role played between ATO and the $IrO_x$ particles. Most recently, Saveleva et al. (2020) used *operando* XPS to study metallic iridium deposited on ATO aerogel to show that during OER, there was a diminution of the Ir(III) phase (the iridium oxidation state most closely associated with degradation by dissolution), and compared to unsupported iridium oxide, much less iridium was lost from the OER via dissolution, confirmed by the use of online ICP-OES. The above literature findings thus strongly suggest that there is an interactive role between $IrO_x$ and ATO during oxygen evolution.

## 2.5 METHODS FOR THE SYNTHESIS OF OXIDE-SUPPORTED CATALYSTS

### 2.5.1 Wet Synthesis

Wet chemistry methods have been used extensively for the synthesis of $IrO_x$/ATO catalysts using Adams' fusion (Puthiyapura et al., 2014; Liu et al., 2015), the polyol method (Oh et al., 2016), chemical reduction (Oh et al., 2015; Solà-Hernández et al., 2019), colloidal synthesis (Tong et al., 2017), microwave-assisted hydrothermal deposition (Massué et al., 2017), and most recently, a solvothermal method to deposit iridium oxide on macroporous ATO (Böhm et al., 2019). With the exception of the Adams' fusion method, it was seen that all the other reported methods were able to deposit small (2-5 nm) $IrO_x$ particles onto ATO support, where methods based on Adams' fusion achieved larger $IrO_x$ particles sizes of 5-8 nm, especially at iridium loadings of lower than 50 wt.% Ir.

It has been shown that post-synthesis heat treatment to catalysts prepared by wet synthesis methods provides fortification of the catalyst-support interface, which results in higher OER activity and stability in these catalysts, as compared to un-calcined catalytic materials (Spöri et al.,

2017). While calcination is necessary for fortification of the interaction between the catalyst and the support, these heat treatments usually cause particle growth; as the material heats up, the particles become more and more mobile and start to migrate towards one another (Munnik, De Jongh & De Jong, 2015). $IrO_x$/ATO catalysts prepared by the Adams' fusion, chemical reduction, polyol, solvothermal and colloidal methods, mentioned above, each contain a calcination step, usually between 300-500°C; while such a step is beneficial for the overall properties of the synthesised catalytic materials, calcination is likely to cause $IrO_x$ particle agglomeration.

Furthermore, it should be noted that in some $IrO_x$/ATO deposition methods, the ATO support is only contacted with $IrO_x$ after the $IrO_x$ particles have been independently synthesised (Oh et al., 2015, 2016; Böhm et al., 2019). This can be problematic in that the interaction between the catalyst ($IrO_x$) and the support (ATO) in these cases is much more superficial in nature than it would be in instances where the catalyst has been synthesised in the presence of the support material (Munnik, De Jongh & De Jong, 2015; Spöri et al., 2017).

The iridium loadings in the aforementioned wet-synthesised $IrO_x$/ATO catalytic materials range from 15-40 wt. % Ir, and this suggests that deposition techniques which are able to provide high OER performance and durability while simultaneously offering iridium low iridium loadings in the range of 1-15 wt.% should be pursued, in order to truly reduce the noble metal content in supported OER catalytic materials.

### 2.5.2 Organometallic Chemical Deposition

An in-house developed, organometallic chemical deposition (OMCD) technique was proven to be highly effective for the preparation of high-performing, carbon, carbide and oxide-supported platinum electrocatalysts for hydrogen and direct methanol fuel cell applications (Taylor et al., 2016; Jackson, Conrad & Levecque, 2017; Mohamed et al., 2018). The method uses the decomposition of platinum acetylacetonate ($Pt(acac)_2$) to deposit platinum nanoparticles onto various support materials by the optimisation of the gas environment and temperature used for the reaction.

This method offers simplicity in comparison to traditional wet chemistry techniques which contain numerous processes and post-treatment steps, as well as offers the advantage of being able to control particle size and morphology of catalysts by manipulation of synthesis conditions (Jackson, Conrad & Levecque, 2017). In the context of Pt/ATO catalysts, notably, the OMCD method resulted in outstanding spatial dispersion of Pt particles over the ATO support, resulting in excellent mass-specific electrochemically active surface area, in comparison to wet synthesis approaches, particularly in the case of 5 wt.% Pt/ATO that was prepared by this method (Mohamed et al., 2018).

#### *2.5.2.1 Organometallic Chemical Vapor Deposition using $Ir(acac)_3$*

Iridium acetylacetonate ($Ir(acac)_3$) is a popular precursor for techniques based on organometallic chemical deposition and has been shown to decompose to iridium or iridium oxide depending on the temperature, gas environment and deposition surface being used for the reaction (Garcia & Goto, 2003; Silvennoinen, Jylhä, Lindblad, Österholm, et al., 2007; Nassreddine et al., 2010; Hämäläinen, Ritala & Leskelä, 2014; Vasilyev et al., 2015). It has been shown that $Ir(acac)_3$ vaporises in vacuum from 150-200°C (Sun et al., 1999; Garcia & Goto, 2003; Kemell et al., 2006; Silvennoinen, Jylhä, Lindblad, Sainio, et al., 2007; Walsh et al., 2009). ***Table 2-1*** below summarises the temperatures and reaction products for the decomposition of $Ir(acac)_3$ in oxygen and argon deposition environments.

***Table 2-1:*** *Summary of decomposition temperatures and reaction products in oxygen and argon environments.*

| Deposition Medium | Decomposition Temperature | Decomposition Products |
|---|---|---|
| Oxygen | $T \geq 250$°C (Garcia & Goto, 2003; Hamalainen et al., 2008; Nassreddine et al., 2010) | $CO_2$, $H_2O$ (Nassreddine et al., 2010) |
| Argon | $T \geq 370$°C (Nassreddine et al., 2010) | $H_2$, CO, $CO_2$, $CH_4$ (Nassreddine et al., 2010) |

Iridium deposition in argon using $Ir(acac)_3$ was found to contain up to 20 wt% carbon, however, deposition in oxygen resulted suppression of the formation of iridium-carbon composites (Garcia & Goto, 2003). It was seen that unless the oxygen flow rate in the deposition process was carefully controlled, iridium oxide would be the dominating iridium species formed during deposition in the presence of oxygen reactive gas (Garcia & Goto, 2003).

# Chapter 3: Research Approach

*In this chapter, a hypothesis is presented to guide the overall approach taken in the thesis, based on the review of literature from Chapter 2. Objectives and key questions to be answered are highlighted.*

## 3.1 RESEARCH OBJECTIVES

The objectives of this thesis are to:

(1) Examine the use of the OMCD method using $Ir(acac)_3$ to produce $IrO_x$ supported onto ATO support
(2) Understand the effect of deposition atmosphere (inert or oxidising) on the physical and electrochemical properties of the synthesised catalysts
(3) Determine the effect of the deposition temperature on the physical and electrochemical properties of the synthesised $IrO_x$/ATO catalysts
(4) Investigate the reproducibility of the OMCD method for $IrO_x$/ATO synthesis
(5) Evaluate strategies for the optimisation of the OMCD technique.

## 3.2 SUMMARY OF KEY LITERATURE FINDINGS

PEM electrolysis is a promising route for the generation of hydrogen by renewable energy, however at present, the commercialisation of this technology is severely hindered by the large capital cost associated with electrolyser anodes, which require large quantities of Ir or Ru-based catalytic materials to catalyse the sluggish oxygen evolution reaction (de Vasconcelos & Lavoie, 2019).

ATO-supported iridium-based electrocatalysts have proven themselves to be highly effective OER catalysts; they are able to exhibit high OER mass-specific activity, while simultaneously utilising much less iridium than is required by unsupported iridium-based OER catalysts. Various wet synthesis techniques have been explored in literature for the synthesis of ATO-supported iridium or iridium oxide nanoparticles for the oxygen evolution reaction (Puthiyapura et al., 2014; Liu et al., 2015; Oh et al., 2015, 2016; Massué et al., 2017; Tong et al., 2017; Böhm et al., 2019; Solà-Hernández et al., 2019). While these methods have been successful in synthesising these materials, they often require numerous steps, and typically a calcination step to strengthen the bond between the catalyst and ATO support. While calcination is necessary, it tends to cause particle agglomeration. Furthermore, some wet synthesis methods combine the ATO support with independently synthesised $IrO_x$ particles (Oh et al., 2015, 2016; Böhm et al., 2019), and this can cause a superficial attachment between the catalyst and support.

An OMCD method was found to be highly successful in the deposition of Pt nanoparticles on carbon, carbide and oxide support materials (Taylor et al., 2016; Jackson, Conrad & Levecque, 2017; Mohamed et al., 2018) with a narrow size range and high spatial dispersion. As ATO has

been shown to interact with $IrO_x$ in a manner that improves the overall OER performance of supported $IrO_x$/ATO catalysts (Oh et al., 2016; Saveleva et al., 2020), the fact that the OMCD method is a purely thermal deposition process suggests that the use of such a method could result in superior fortification of the $IrO_x$-ATO interface, while simultaneously avoiding the unnecessary migration of nucleated particles, resulting in OER performance which surpasses the performance of similar materials prepared by traditional wet synthesis methods. In addition, OMCD is a one-step method that offers simplicity in comparison to wet chemistry techniques which contain numerous process and post-treatment steps.

## 3.3 HYPOTHESIS

It is hypothesised, that the application of the OMCD method which was successfully utilised to deposit Pt nanoparticles on ATO and other supports can be extended to the deposition of $IrO_x$ supported on ATO, using the decomposition of $Ir(acac)_3$. Furthermore, the manipulation of the deposition temperature and reaction environment can be used to tune physical properties, and thus electrochemical performance of the catalysts.

## 3.4 KEY QUESTIONS

(1) How does temperature affect OER mass-specific activity across oxidising and inert synthesis conditions?
(2) How does the performance of the synthesised catalysts compare to a commercially available state-of-the-art OER catalyst?
(3) Can the deposition of $IrO_x$ on ATO be reproduced reliably based on iridium loading and OER performance attained?
(4) How can the existing synthesis method be developed to improve the deposition process?

# Chapter 4: Experimental Part I – Catalyst Synthesis and Physical Characterisation

*This chapter details the experimental programme which was undertaken to synthesise and physically characterise $IrO_x$/ATO electrocatalysts, prepared by organometallic chemical deposition. The physical characterisation techniques which were used to understand the behaviour of the synthesised materials are explained.*

## 4.1 CATALYST SYNTHESIS BY ORGANOMETALLIC CHEMICAL DEPOSITION

### 4.1.1 Apparatus and Chemicals

***Table 4-1***below outlines the various materials which are used for the synthesis of $IrO_x$/ATO catalysts, using the organometallic chemical deposition (OMCD) technique, and ***Figure 4-1*** shows all the apparatus involved in the deposition process.

***Table 4-1:*** *OMCD $IrO_x$/ATO chemicals information.*

| Name | Chemical Formula | Information | Supplier |
|---|---|---|---|
| Iridium (III) Acetylacetonate | $C_{15}H_{21}IrO_6$ ($Ir(acac)_3$) | Purity: 97% | Sigma-Aldrich Product number: 333352 |
| Antimony Tin Oxide (ATO) Nanopowder | $Sb_{0.1}Sn_{0.9}O_2$ | 30 nm particle size $SnO_2$:$Sb_2O_3$ = 90:10 wt.% Purity: 99.95+% | US Research Nanomaterials Inc. Product number: US3800 |
| Oxygen | $O_2$ | Grade: Research 5.0 | Air Liquide |
| Argon | Ar | Purity: 99.999% | Air Liquide |

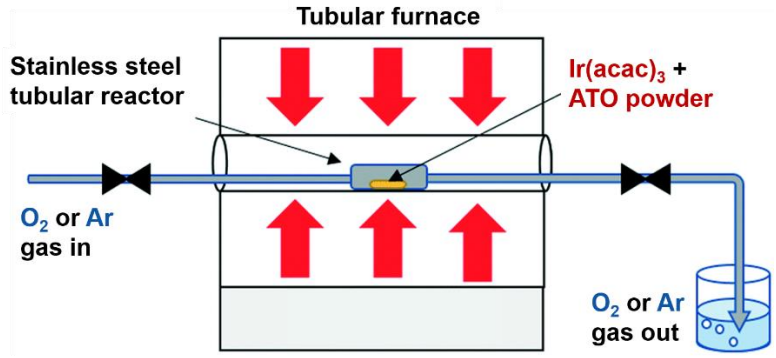


***Figure 4-1:*** *Diagram to show OMCD catalyst preparation in a tubular furnace, adapted from* (Mohamed et al., 2018).

### 4.1.2 Synthesis Procedure

For all catalyst synthesis, ATO nanopowder was used as the support material and iridium (III) acetylacetonate, $Ir(acac)_3$, was used as the organometallic precursor for the deposition process. All catalysts were prepared using an OMCD method. Two nominal catalyst loadings of 5 wt.% and 20 wt.% Ir were prepared during the course of this work; ***Table 4-2*** below shows the respective masses of ATO and $Ir(acac)_3$ that were used to prepare each of these theoretical catalyst loadings.

***Table 4-2:*** *Masses of ATO and $Ir(acac)_3$ used for catalyst preparation.*

| Nominal Iridium Loading in Catalyst | Mass of ATO /mg | Mass of $Ir(acac)_3$ / mg |
|---|---|---|
| 5 wt.% | 5000.00 | 692.00 |
| 20 wt.% | 200.00 | 132.00 |

The solid powder ATO+$Ir(acac)_3$ mixture was crushed using a mortar and pestle and placed inside a 20 mL stainless steel reactor vessel which was inserted into a tubular furnace. The first and second stages of the process involve the removal of water from the ATO+$Ir(acac)_3$ mixture by heating the reactor vessel to 120°C and holding at this temperature for half an hour; during this process the reaction gas, oxygen or argon, was flowed through the reactor tube at 20 mL $min^{-1}$ to flush the reaction volume. The reaction chamber was then sealed, enclosing reaction gas and the dry ATO+$Ir(acac)_3$ mixture. The vessel was heated to the desired temperature for deposition, and held at this temperature for a period of 2 hours, after which it was allowed to cool down to room temperature before collection of the $IrO_x$/ATO electrocatalyst powder. A schematic representation of the deposition process can be seen in ***Figure 4-2*** below.

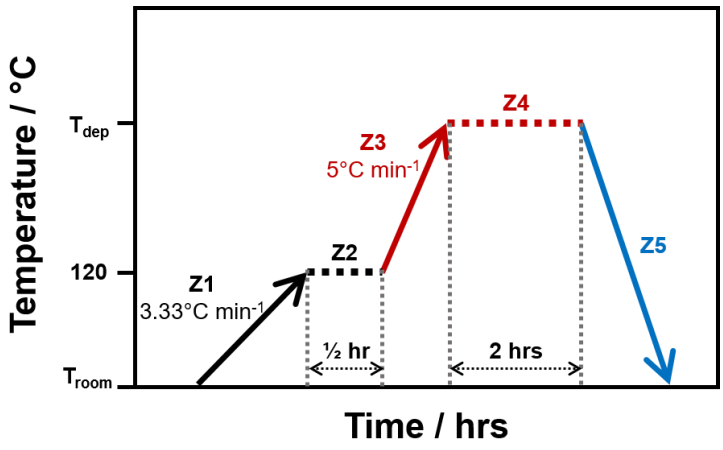


***Figure 4-2:*** *Schematic representation of the OMCD process. Z1 and Z2 indicate the removal of water from the ATO+Ir(acac)₃ mixture by heating the reactor vessel to 120°C and holding at this temperature for half an hour; the vessel is then heated to the desired deposition temperature (Z3) and is held here for a period of 2 hours (Z4), after which the reactor is allowed to cool down to room temperature (Z5) before collection of the $IrO_x$/ATO catalyst powder.*

## 4.2 PHYSICAL CHARACTERISATION

### 4.2.1 X-ray Diffraction

X-ray diffraction is the elastic scattering of X-ray photons as they interact with periodically ordered matter (crystalline structures), in directions which fulfil Bragg's Law (Che & Védrine, 2012). This is a common characterisation technique in heterogeneous catalysis, which is used to analyse the bulk structure of crystalline, solid materials. This technique can also be utilised to determine the crystallite size of a given material provided that its particle size exceeds the detection limit (~3 nm) for XRD (Niemantsverdriet, 2007; Che & Védrine, 2012).

XRD was used for the structural characterisation of the OMCD $IrO_x$/ATO catalysts in this work, using a Bruker D8 Advance diffractometer operating at 40 kV with a Co-$K_\alpha$ radiation source. These measurements were performed at the University of Cape Town.

### 4.2.2 Techniques Based on Electron Microscopy

The interaction of an incident electron beam with a sample leads to various different types of signals being emitted (Niemantsverdriet, 2007). These signals can be analysed to collect unique pieces of information relating to the structure of the sample. ***Figure 4-3*** below shows the different types of signals which can be emitted, as well as the techniques which would be utilised to measure these signals.

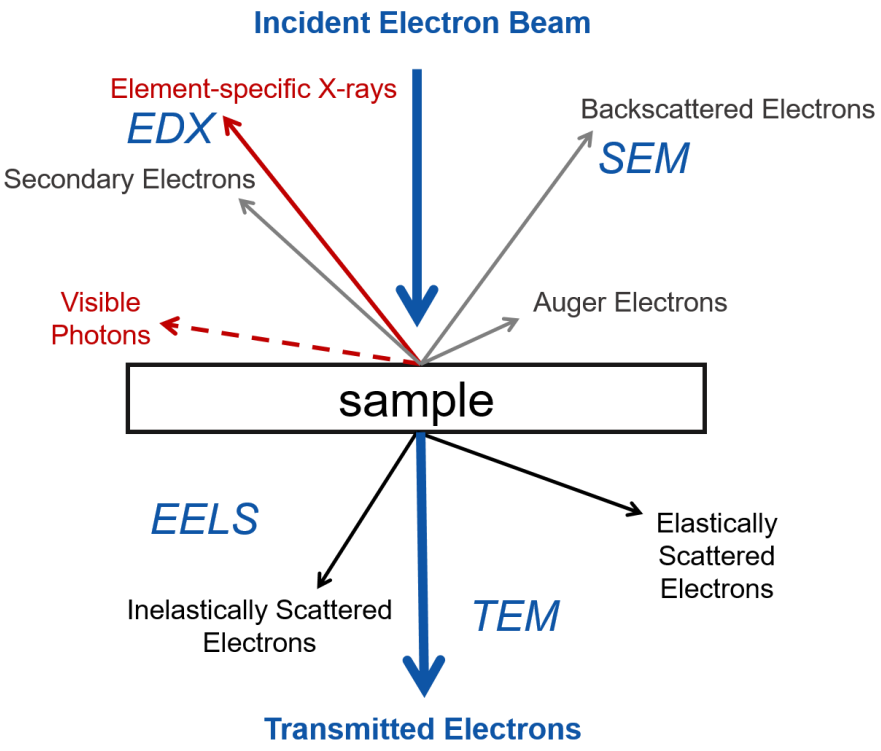


***Figure 4-3:*** *Schematic illustrating how the incident electron beam interacts with the sample, causing the release of a number of detectable signals.*

#### *4.2.2.1 High-resolution Scanning Transmission Electron Microscopy*

High-resolution scanning transmission electron microscopy (HR-STEM) operates using a combination of transmission and scanning microscopy modes. A focussed beam of electrons is scanned over the sample, and a signal is collected to form an image (Che & Védrine, 2012). High quality spatial resolution is achieved by measuring signals from transmitted electrons, in addition to backscattered electrons (Rozmus, Blicharski & Dymek, 2006). The transmitted beam is included in the bright field detector so that holes in the collected images appear as 'bright', whereas, the annular dark field (ADF) detector excludes the transmitted electrons so that the holes appear 'dark' (Rozmus, Blicharski & Dymek, 2006). ***Figure 4-4*** below shows a schematic representation of HR-STEM.

A high angle annular dark field (HAADF) detector enhances the contrast on the collected image to show the presence of atoms of high atomic number elements (Rozmus, Blicharski & Dymek, 2006). For example, in HRSTEM imaging of $IrO_x$ nanoparticles supported on ATO support, the HAADF detector enhances the contrast of the iridium containing particles on dark field images, as iridium is of a higher atomic number than antimony and tin.

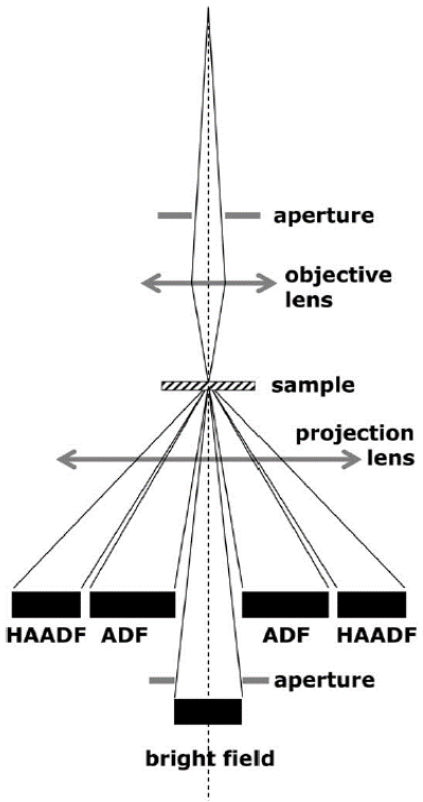


***Figure 4-4:*** *A schematic representation of HR-STEM, where HAADF and ADF stand for high-angle annular dark field and annular dark field, respectively; taken from Niemantsverdriet (2007).*

All HR-STEM measurements were performed by Richard Martin and Patricia Kooyman at the Nelson Mandela Metropolitan University, using a JEOL JEM ARM200F double Cs-corrected electron microscope, equipped with a field emission gun (FEG), and a HAADF detector, operated at 200 kV. An Oxford XMax 100 TLE detector was used for elemental mapping to gain a qualitative understanding of the iridium dispersion. Image J was used as a counting tool to quantify the particle sizes of the $IrO_x$ nanoparticles. At least 150 particles were counted to obtain normalised particle size frequency histograms, and it was ensured that the Ferret diameter, the maximum length across a non-spherical particle, was measured for particle size. Normalisation of these histograms was done with respect to the number of particles counted. The d-spacings of $IrO_x$ particles were extracted from the visible lattice fringes on HR-STEM images, using the plot profile function in Image J software.

#### *4.2.2.2 Energy Dispersive X-ray Spectroscopy (EDX)*

As shown in ***Figure 4-3***, upon the interaction of an incident electron beam with a sample, various detectable signals are evolved. The emission of characteristic, element-specific X-rays from a sample can be analysed to provide quantitative information pertaining to the composition of the material (Niemantsverdriet, 2007; Che & Védrine, 2012).

One of the challenges faced in this work was in the reliable determination of the Ir mass-content in the synthesised $IrO_x$/ATO catalysts. As the samples could not be digested completely in aqua regia (not even with the addition of hydrofluoric acid), inductively coupled plasma optical emission spectroscopy (ICP-OES) could not be used as a meaningful quantification technique. Energy dispersive X-ray spectroscopy (EDX) was therefore applied to quantify the mass of iridium present in the synthesised electrocatalysts. A scanning electron microscope (SEM), FEI Nova Nano SEM 230 with a field emission gun (FEG) was used to collect the EDX spectra, and all spectra were collected at 20 kV using an Oxford X-Max detector and INCA software.

### 4.2.3 X-ray Photoelectron Spectroscopy (XPS)

X-ray photoelectron spectroscopy (XPS) is a surface-sensitive technique which can be used to determine the composition of a material, based on the analysis of characteristic, element-specific electron binding energies (Niemantsverdriet, 2007). XPS is based on the photoelectric effect, where incident X-rays are absorbed and photoelectrons, with a kinetic energy characteristic to a particular element, are ejected from the sample and analysed. See ***Figure 4-5*** for a visual representation of this.

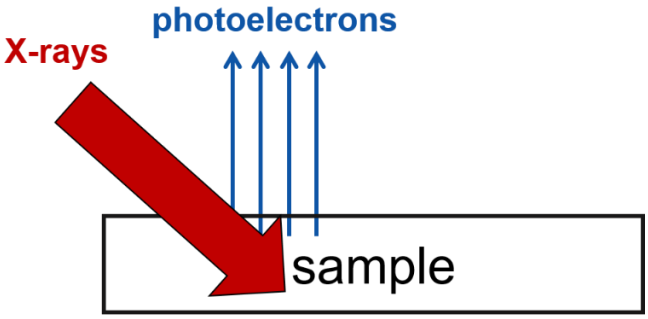


***Figure 4-5:*** *Interaction of incident X-rays with a sample during XPS.*

To gain an understanding of the iridium oxidation states present in IrOx/ATO, XPS measurements were performed by Bryan Doyle and Emanuella Carleschi at the University of Johannesburg. A PHOIBOS 150 electron analyser (SPECS GmbH) together with a monochromated Al $K_\alpha$ source (1486.71 eV) was used. The energy resolution was set to 0.7 eV for survey spectra and 0.5 eV for all other spectra. The charging of the sample surface was compensated by shining the samples with low energy electrons produced by a low-energy electron flood gun, where the electron energy was 2 eV, and the electron flux was 20 μA.

XPSPeak4.1 software was utilised for fitting of the Ir 4f and O 1s components, using an approach that is an agreement with previously published work by Pfeifer et al. (2016) and Yu et al. (2018). For Ir 4f, a Lorentzian/Gaussian ratio of 20 was used for all components. A full width at half maximum (FWHM) of 1.2 eV was used for $Ir^{4+}$ and $Ir^{3+}$, 2.4 eV was applied for the satellite peaks occurring at 62.8 eV and 63.3 eV, and 1.7 eV for satellite peak at 67.8 eV. All photoelectron peaks were fit using TS and TL asymmetry factors of 0.2 and 100.

For the O 1s spectrum, first, the contribution from an overlapping component Sb $3d_{5/2}$ at 541.0 eV was determined using the area measurement under Sb $3d_{3/2}$ at 540.4 eV, and taking into account the area ratios between $3d_{5/2}$ and $3d_{3/2}$. All oxygen components were then fit with a FWHM of 1.5 eV and Lorentzian/Gaussian ratio of 20. Asymmetry factors of 0.1 and 100 were applied for Sb $3d_{5/2}$, as well as for oxygen bonded to metallic components.

### 4.2.4 Thermogravimetric Studies

Thermogravimetric experiments were conducted to understand the phase change processes of the $Ir(acac)_3$ precursor. A METTLER TGA/sDTA851e Thermogravimetric Analyser at the University of Cape Town was used and 10.0 mg of the precursor was inserted into an alumina heating pan. 10.0 mL $min^{-1}$ of synthetic air was flowed through the analyser. The temperature was ramped from ambient conditions to 650°C at a heating rate of 5° $min^{-1}$.

# Chapter 5: Experimental Part II – Electrochemical Characterisation

*In this chapter, the electrochemical set-up and protocol that was used to measure the oxygen evolution performance of the synthesised $IrO_x$/ATO catalysts are explained. Furthermore, the two types of data analysis which were used in the evaluation of catalyst performance are discussed, and a justification is given for the mass-normalisation of the measured current responses. The study of a commercial OER catalyst is used to validate the electrochemical test set-up and OER testing protocol.*

## 5.1 THE ELECTROCHEMICAL TEST SET-UP

It should be noted that prior to all electrochemical measurements, it was ensured that Nochromix® cleaning solution (concentrated $H_2SO_4$ and Nochromix® oxidising agent) was utilised to clean the experimental glassware. This was done to eliminate the presence of any organic and metallic contaminants. All clean glassware was stored in ultrapure 18 MΩ Millipore distilled water. ***Figure 5-1*** below illustrates the experimental set-up used for all OER electrochemical characterisation.

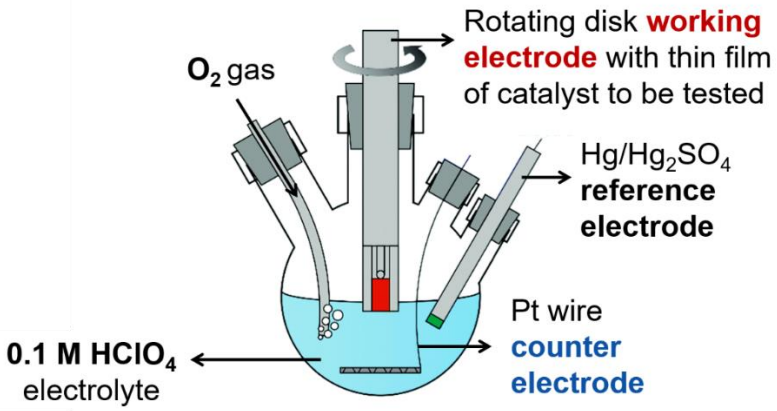


***Figure 5-1:*** *Electrochemical testing set-up.*

The three-electrode cell set-up was used with 0.1 M perchloric acid as the acidic electrolyte. An $Hg/Hg_2SO_4$ reference electrode was used for the experiments because it is stable and has a well-defined potential in perchloric acid. It was ensured that before any characterisation was performed, the reference electrode had been calibrated in hydrogen-saturated, 0.1 M perchloric acid electrolyte. This was done to ensure that all potentials applied to the working electrode in the experiments were measured and known against the reversible hydrogen electrode (RHE). A platinum wire counter electrode of substantially larger surface area than the working electrode was used to ensure that there was no limitation of the current at the counter electrode (Wei et al., 2019).

Pt is particularly suitable for OER because on this electrode, hydrogen evolution takes place, and as the electrolyte is continuously bubbled with oxygen, the evolved hydrogen is rapidly removed from the counter electrode, preventing interference at the working electrode. The counter electrode was cleaned before each use by flame sterilisation, followed by rinsing in ultrapure 18 MΩ Millipore distilled water.

Electrochemical characterisation was performed using a Biologic-SP300 double channelled potentiostat, where data was collected using EC-Lab software. A rotating disk electrode (RDE) set-up (150 mL glass cell, PINE Research) and 100 mL of 0.1 M perchloric acid electrolyte (prepared from 60% stock solution from Kanto Chemical Company) were used for all electrochemical tests. Three working electrodes were prepared and characterised for each catalyst that was tested, to estimate the error of the results.

A large number of $O_2$ bubbles evolve at high potentials (1.600 V vs. RHE onwards), and these bubbles can block active electrochemical reaction sites. Rotation is beneficial for the removal of evolved bubbles to retain the accuracy of the measurement (Garcia & Koper, 2018); the working electrode was therefore rotated at 1600 rpm for this purpose. To further improve the bubble removal, which was particularly necessary for the stability portion of the testing protocol, the RDE set-up was tilted at an angle between 15-30°.

## 5.2 CHOICE OF OER PERFORMANCE DESCRIPTOR

Normalisation of the current responses obtained in all the electrochemical experiments performed in this work was done with respect to the mass of iridium present on the RDE. Normalisation by geometric surface area of the RDE is not applicable for this purpose as it does not account for electrode loading effects. Normalisation by the electrochemically active surface area or the turn-over frequency are also not feasible for iridium-based OER catalysts. Several works in the past few years which have strived to better understand the mechanism of oxygen evolution on iridium oxides have shown that on such materials, the reaction is not a surface reaction, but rather that it is a sub-surface reaction with participation from oxide lattice oxygen species (Binninger et al., 2015; Pfeifer, Jones, Wrabetz, et al., 2016; Grimaud, Diaz-Morales, et al., 2017; Saveleva et al., 2018). As normalisation metrics such as the turn-over frequency and the electrochemically active surface area account for only surface participation of the catalyst, these descriptors are not suitable as OER performance descriptors. Therefore, the most reasonable normalisation of the experimental current responses can at present only be done relative to the mass of iridium on the RDE (Fabbri et al., 2014; Wei et al., 2019). In addition, as iridium is commercially available on a mass basis, normalisation by mass offers the most technically relevant comparison of OER performance across different catalytic materials.

## 5.3 ACTIVITY AND STABILITY TESTING PROTOCOLS

All electrodes were subjected to cyclic voltammetry (CV) at the beginning of the electrochemical protocol to clean and activate the catalyst layer. For this purpose, 10 potential cycles were carried out from 1.000-1.400 V vs. RHE at 50 mV $s^{-1}$, followed by a further 10 cycles in the same potential range, at 10 mV $s^{-1}$. Thereafter, the catalyst was subjected to successive activation steps using chronoamperometry from 1.400-1.480 V vs. RHE in 20 mV steps, for a duration of 1 minute per step. Chronoamperometry was also utilised for measuring OER activity and stability: the potential was stepped up from 1.500-1.560 V vs. RHE holding for 1 minute per step. To remove the effect of transient capacitive currents, only the last 30 seconds of each step were used for OER activity analysis, because the currents in this portion of the measurement are assumed to be controlled predominantly by the OER reaction kinetics (Fabbri et al., 2014).

Electrochemical impedance spectroscopy (EIS) was performed at 1.000 V vs. RHE in the frequency range from 200 KHz to 100 mHz to determine the effective ohmic resistance used for iR-correction.

The stability of the electrocatalysts was evaluated by applying a potential of 1.600 V vs. RHE for a period of 2 hours, after which the catalyst was again subjected to the OER activity protocol (described above) to determine the relative loss of mass-specific activity. Potentials exceeding 1.600 V vs. RHE were not explored for stability measurements: at these potentials, the OER reaction rate was so high that large numbers of $O_2$ bubbles were produced within the porous catalyst layer, causing blocking and detachment of the catalyst from the glassy carbon electrode.

## 5.4 DATA ANALYSIS

There were two types of data analysis which were utilised during the course of this project. The first was a rapid method to accurately screen electrocatalysts in order to make quick and informed decisions about the direction of the work, without compromising on the quality. To do this, the mass-activity of all the prepared catalysts was screened at an applied potential of 1.525 V vs. RHE, using chronoamperometry. The second type of analysis used in this work was a detailed Tafel slope analysis, where data points gathered from chronoamperometry between 1.500 and 1.560 V vs. RHE were used to plot a Tafel slope of iR-free potential versus mass-specific activity. Following this, the mass-specific activity of a given catalyst could be extracted for any potential that was included in the plotted range, using interpolation/extrapolation of the Tafel slope equation. This approach was particularly useful in making comparisons to literature and commercial catalyst data, where the mass-specific OER activity is reported at a variety of potentials. Regardless of which of these two approaches was utilised, the initial data processing steps are identical: these are the reference and ohmic corrections, as well as the conversion of the current response to an iridium-based mass-specific OER activity. The steps involved in the OER data processing for this work are summarised in the schematic representation seen in ***Figure 5-2*** below. It should be noted that

regardless of the analysis approach taken, the electrochemical protocol (as described above) was the same for all measurements.

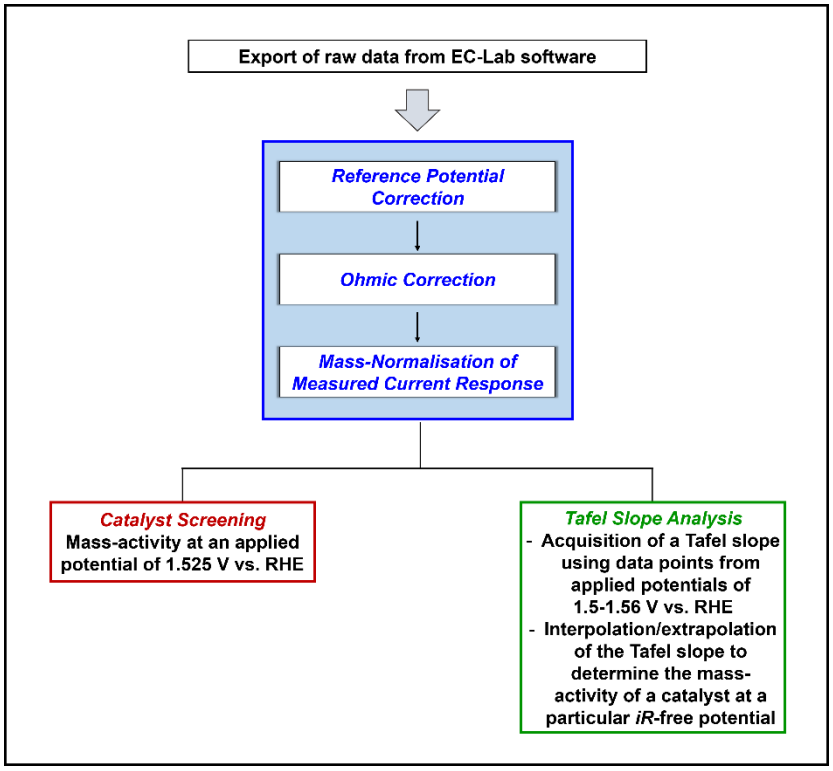


***Figure 5-2:*** *Schematic representation of the various steps which need to be taken in the analysis of data.*

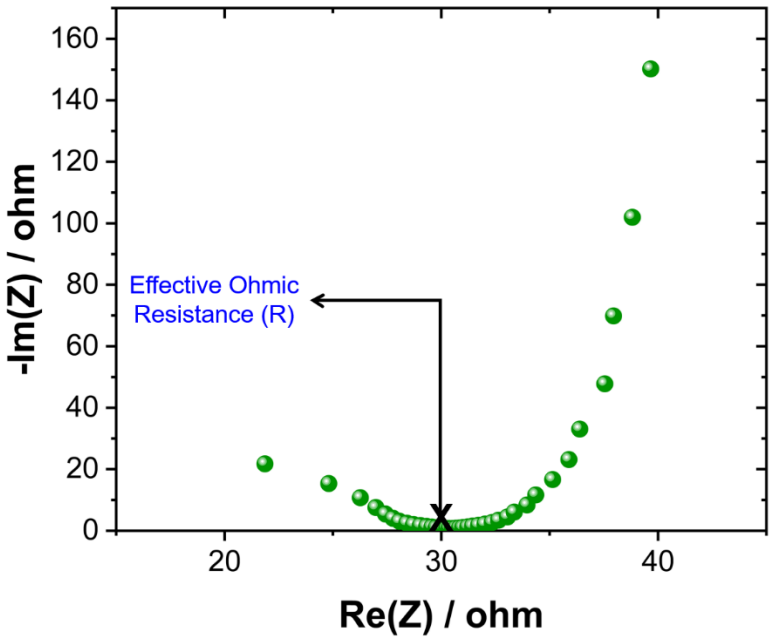


***Figure 5-3:*** *Effective ohmic resistance (R), from a Nyquist plot at 1.000 V vs. RHE, in a frequency range of 200 kHz to 100 mHz.*

The process of converting the raw data acquired by EC-Lab into mass-normalised OER data requires a number of steps. To begin with, all the applied potentials are transformed into potentials

versus the reversible hydrogen electrode (RHE). After this, an ohmic correction is performed on these reference-transformed potentials to compensate for potential drop between the working and reference electrodes, to acquire the true potential which was applied to the working electrode. This is a particularly important step to be taken in the analysis of electrochemical data, as at high current densities fairly large ohmic losses are observed, and failure to correct for this can result in severe inaccuracies in data analysis and interpretation. ***Figure 5-3*** above shows the extraction of the effective ohmic resistance (R) from a Nyquist plot, obtained from electrochemical impedance spectroscopy, measured at 1.000 V vs. RHE.

The equation below, ***Equation 5-1***, illustrates how to convert reference-corrected potentials into ohmic-free (*iR-free*) potentials using the effective ohmic resistance (R).

***Equation 5-1***

$$iR - free\ Potential\ = Applied\ Potential\ - Potential\ Drop$$

$$where, Potential\ Drop\ = i\ \times\ R$$

The final step of the initial data processing involves the conversion of the current response into mass-specific activity, by normalisation of these currents with respect to the mass of iridium present on the RDE. This mass is calculated from the iridium mass percentage in the catalyst, determined by EDX as described previously. The calculation for this can be seen in ***Equation 5-2*** below.

***Equation 5-2***

$$m_{Ir,\ electrode} = \frac{V_{ink\ deposited\ on\ electrode}}{V_{total\ ink\ volume}} \times m_{catalyst\ in\ total\ ink\ volume} \times\ Mass\ fraction\ of\ Ir\ in\ catalyst$$

## 5.5 WORKING ELECTRODE PREPARATION

### 5.5.1 $IrO_2$-$TiO_2$ (Elyst Ir75) Commercial Benchmark

Porous, thin-film electrodes were prepared to have a catalyst loading of 100 $\mu g_{cat}$ $cm^{-2}$ from ink dispersions that were drop-cast onto 0.196 $cm^2$ glassy carbon electrode disks. An electrode catalyst loading of $100_{cat}$ $\mu g$ $cm^{-2}$ was explored for its similarity to the loadings reported for the same commercial benchmark in literature, making this loading suitable for the validation of the electrochemical testing set-up and protocol, as well as for the comparison to the synthesised catalyst materials. The inks consisted of 4.00 ml of isopropanol, 1.00 ml of water, 20 µl of Nafion® ionomer solution (5 wt.% in water and aliphatic alcohols, Fuel Cell Earth), and 10 mg of a commercial $IrO_2$-$TiO_2$ OER catalyst (Elyst Ir75, Umicore AG & Co. KG). These inks were ultra-sonicated for 30 mins before deposition onto glassy carbon electrodes. The ink was collected by a micropipette while undergoing magnetic stirring; this was done to ensure that the ink deposited on the electrode was always well-dispersed so that the mass of iridium deposited on each electrode

could be calculated reliably. A quantity of 10 μl of catalyst ink was deposited to attain an electrode loading of 100 $\mu g_{cat}$ $cm^{-2}$. The ink was deposited onto each glassy carbon disk, and dried stationary at room temperature in air.

### 5.5.2 OMCD $IrO_x$/ATO Catalysts

Porous, thin-film electrodes were prepared to have a catalyst loading of 400 $\mu g_{cat}$ $cm^{-2}$, from ink dispersions that were drop-cast onto 0.196 $cm^2$ glassy carbon electrode disks. As the normalisation of all measured current responses was done with respect to the mass of iridium present on the electrodes, 400 $\mu g_{cat}$ $cm^{-2}$ was used as an electrode loading to test the prepared catalysts because this loading would offer a similar iridium content to electrodes which were prepared for testing of the commercial benchmark, based on the nominal loading of 20 wt.% Ir which was utilised to prepare the OMCD $IrO_x$/ATO catalysts, using both the nominal and actual Ir loadings of these catalysts. While the actual iridium loadings of the catalysts differ from the nominal loading, the electrode loadings used in this work were selected based on the nominal iridium loading in the prepared catalysts. ***Table 5-1*** below illustrates the catalyst and iridium-based electrode loadings of the commercial benchmark and the OMCD $IrO_x$/ATO catalysts. Based on the electrode loadings illustrated in ***Table 5-1***, it can be said that the OMCD $IrO_x$/ATO electrodes consisted of thicker catalyst films on the RDE than that of the commercial benchmark. While the OER itself is not a mass-transport limited reaction, it is possible that evolved oxygen bubbles are not removed as rapidly and efficiently from the pores of the catalyst in the thicker electrode as they are in the thinner electrode case, possibly resulting in an overall lower rate of the OER in thicker electrodes than thinner electrodes of the same catalyst. However, as Ir-based mass-specific OER performance is currently the most sound means to evaluate *ex-situ* catalyst performance, the choices made for electrode loadings in this work are credible, particularly considering that in the worst-case scenario, the activity of the OMCD $IrO_x$/ATO catalysts is likely to be underestimated rather than overestimated. The $IrO_x$/ATO catalyst inks consisted of 1.00 ml of water, 4.00 ml of ethanol, 20 μl of Nafion® ionomer solution (5 wt.% in water and aliphatic alcohols, Fuel Cell Earth), and 10 mg of the $IrO_x$/ATO catalyst. These inks were ultra-sonicated for 30 mins before deposition onto glassy carbon electrodes. The ink was collected by a micropipette while undergoing magnetic stirring; this was done to ensure that the ink deposited on the electrode was always well-dispersed. A quantity of 40 μl of catalyst ink was deposited onto each glassy carbon disk, and dried stationary at room temperature in air.

***Table 5-1:*** *Catalyst and iridium-based electrode loadings for the $IrO_2$-$TiO_2$ commercial benchmark and the OMCD $IrO_x$/ATO catalysts based on the nominal and actual Ir loading of the prepared catalysts.*

| **Catalyst** | **Catalyst Ir loading / wt%** | **Electrode loading (catalyst-based) / $\mu g_{cat}$ $cm^{-2}$** | **Nominal electrode loading (iridium-based) / $\mu g_{Ir}$ $cm^{-2}$** | **Actual electrode loading (iridium-based) / $\mu g_{Ir}$ $cm^{-2}$** |
|---|---|---|---|---|
| $IrO_2$-$TiO_2$ (Elyst Ir75) Commercial Benchmark | 74.4 | 100 | - | 74.4 |
| $O_2$-320°C | 9.4 | 400 | 80.0 | 37.6 |
| $O_2$-420°C | 9.7 | 400 | 80.0 | 38.8 |
| $O_2$-520°C | 12.0 | 400 | 80.0 | 48.0 |
| $O_2$-620°C | 6.4 | 400 | 80.0 | 25.6 |
| Ar-320°C | 11.4 | 400 | 80.0 | 45.6 |
| Ar-420°C | 10.6 | 400 | 80.0 | 42.4 |
| Ar-520°C | 9.3 | 400 | 80.0 | 37.2 |
| Ar-620°C | 4.2 | 400 | 80.0 | 16.8 |
| Ar-720°C | 16.0 | 400 | 80.0 | 64.0 |

## 5.6 BENCHMARKING

A commercial $IrO_2$-$TiO_2$ OER catalyst (Elyst Ir75, Umicore AG & Co. KG) was used as a benchmark to validate the experimental set-up, as well as to gauge the performance of the catalysts in this work in comparison to a commercially available catalyst. Elyst Ir75 has been characterised extensively in literature, allowing for reasonable comparisons to be made.

The Tafel slope analysis method was used for the OER benchmarking of Elyst Ir75 (74.4 wt.% Ir), a well-known commercial catalyst. ***Figure 5-4*** below shows the Tafel slopes attained by the commercial benchmark before and after stability tests. The Tafel slope obtained prior to stability testing was 59 mV $dec^{-1}$, and this changed to 61 mV $dec^{-1}$ after the stability tests were performed. Both Tafel slope values are comparable to 57-60 mV $dec^{-1}$ reported in literature for the same catalyst (Oakton et al., 2017; Spöri et al., 2019). The mass-specific activity of the commercial benchmark at a fixed potential was extracted from the plotted Tafel slopes, in order to make comparisons of the benchmark tested in this work versus in other works. At a potential of 1.525 V vs. RHE, the commercial benchmark achieved a mass-specific activity of 10.4 ± 1.9 $A g^{-1}_{Ir}$, a value which is in close agreement with the findings of Oakton et al. (2017), where at the same potential, a mass-specific activity of 14 ± 4 $A g^{-1}_{Ir}$ was achieved. Elyst Ir75 was evaluated by Spöri et al. (2019) and Böhm et al. (2019) at a potential of 1.53 V vs. RHE, and at this potential, these works measured mass-specific OER activities of 14 $A g^{-1}_{Ir}$ and 8 $A g^{-1}_{Ir}$, respectively; in this work, at a potential of 1.53 V vs. RHE, a mass-activity of 12.6 ± 2.2 $A g^{-1}_{Ir}$ was achieved. As the testing of the Elyst Ir75 commercial benchmark in this work yielded similar results

to those in the works mentioned above, it can be said that both the electrochemical test set-up and the test protocol in this work are valid and reliable.

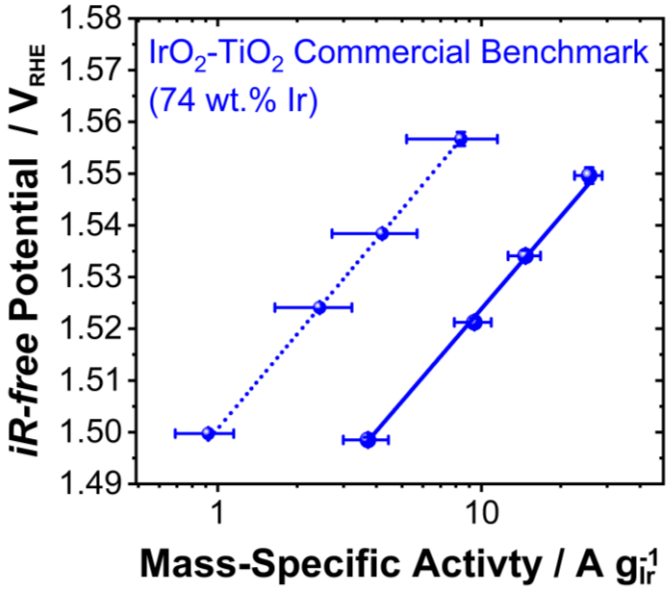


***Figure 5-4:*** *Mass-specific Tafel plots for $IrO_2$-$TiO_2$ (Elyst Ir75) commercial benchmark where the solid line represents initial mass-activity, and the dotted line represents the measurement of mass-specific activity after stability testing.*

# Chapter 6: Organometallic Chemical Deposition of Iridium Oxide on Antimony-Doped Tin Oxide Support

*This chapter explores the deposition of $IrO_x$ on ATO in oxygen and argon reaction environments, in varying temperatures. The iridium precursor is analysed using a thermogravimetric study to understand the phase of the precursor during deposition conditions. A series of catalysts which were prepared using the organometallic chemical deposition method were analysed using energy dispersive X-ray spectroscopy to determine the iridium mass loading in the synthesised materials. These materials were quickly screened for their electrochemical oxygen evolution mass-specific activity in order to down-select which materials should be subject to detailed physical characterisation by X-ray photoelectron spectroscopy, and high-resolution scanning transmission electron microscopy. Detailed explanations to describe the observed oxygen evolution reaction activity were made based on the results obtained from physical characterisation. The two most viable catalysts were then subjected to stability tests, to discern their stability in ex-situ OER conditions.*

## 6.1 UNDERSTANDING THE PHASE OF THE PRECURSOR

Literature studies on the use of $Ir(acac)_3$ as a precursor for the deposition of iridium thin films have claimed that the precursor evaporates between 150-200°C (Sun et al., 1999; Garcia & Goto, 2003; Kemell et al., 2006; Walsh et al., 2009), however as is typical for chemical vapour deposition processes, these studies were performed in vacuum conditions. In principle, the vaporisation temperature ranges reported in literature should hold at atmospheric pressure as well, given that the precursor in our OMCD method has a partial pressure of zero in the in-flowing oxygen gas, because it is introduced to the reaction chamber as a solid. However, thermogravimetric analysis of the $Ir(acac)_3$ precursor was performed (***Figure 6-1*** below) in order to verify whether or not the precursor would evaporate or melt at atmospheric conditions.

Here it was observed that a sharp decline in mass occurs between 200-280°C, and that by 280°C, a virtually complete loss of precursor has occurred. This result would suggest that the precursor vaporises from 200-250°C, a slightly higher temperature range than that observed in literature works using the same precursor for atomic layer and organometallic deposition processes.

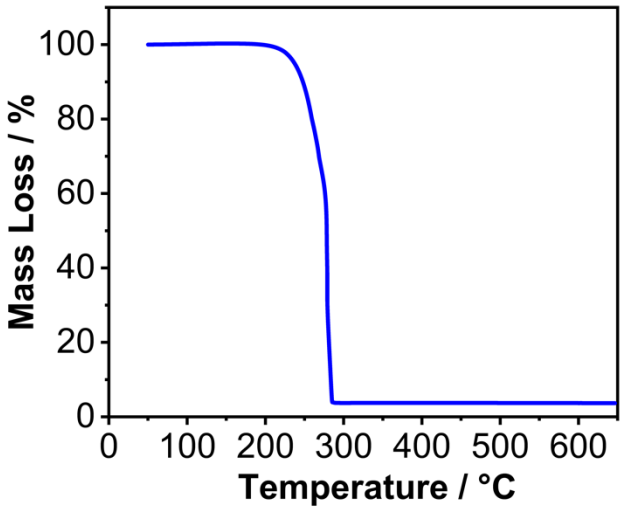


***Figure 6-1:*** *Thermogravimetric analysis of iridium acetylacetonate, showing mass loss from room temperature to 650°C.*

This insight on the behaviour of the precursor also proves that in deposition processes using $Ir(acac)_3$, vaporisation of the precursor would take place before decomposition occurs. Decomposition of the precursor is said to take place from 250°C in oxygen reactive gas, and from 370°C in argon atmosphere (Vargas Garcia et al., 2003). For these reasons deposition temperatures in the range of 300-650°C were explored in oxygen, and temperatures of 300-750°C were explored in argon conditions.

## 6.2 CATALYST SYNTHESIS AND SCREENING

### 6.2.1 Iridium Mass Loading by Energy Dispersive X-ray Spectroscopy (EDX)

#### *6.2.1.1 Method Validation and Calibration*

An $IrO_2$-$TiO_2$ commercial catalyst (Elyst Ir75, Umicore AG & Co. KG), with a known iridium mass content of 74.4 wt.% (as given in the batch specifications), was analysed using EDX; a result of 71.8 ± 1.9 wt.% of iridium was obtained, validating the suitability of this technique to quantify the mass of iridium present in the $IrO_x$/ATO catalysts. To increase the precision of the measurement, a series of internal standards was prepared (ranging from 10 to 50 wt.% Ir) by diluting the commercial $IrO_2$-$TiO_2$ catalyst with Titania. EDX measurements were then taken for each of these standards, and a calibration graph was plotted for the measured Ir wt.% values from EDX, versus the known Ir wt.% from the prepared standards. This calibration plot (***Figure A-1*** in **Appendix A**) was then used to determine the iridium mass loading of OMCD $IrO_x$/ATO using EDX. Here, the measured mass percentage of iridium in the catalyst was corrected using the calibration profile to obtain a more accurate value.

#### *6.2.1.2 Iridium Mass Loading of the Prepared Catalysts*

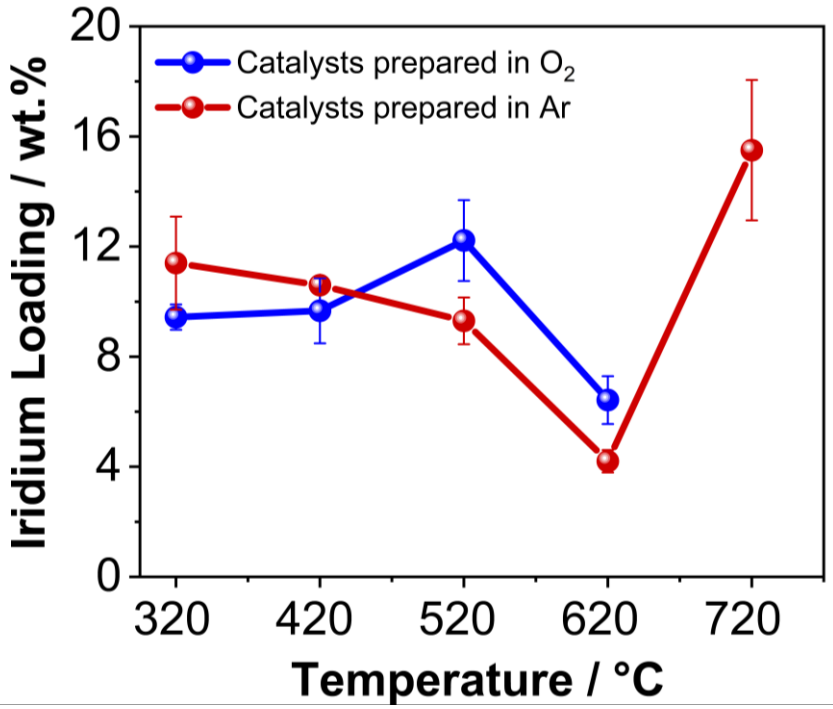


***Figure 6-2:*** *Iridium deposition yield for catalysts prepared in oxygen and argon from 320 to 720°C.*

EDX analysis revealed that while all the OMCD $IrO_x$/ATO catalysts were prepared to have a nominal iridium loading of 20 wt.%, this target loading was not achieved in any of the syntheses, impartial to the gas environment and temperature used for deposition, as seen in ***Figure 6-2*** above. The reasons for these iridium losses during OMCD could be attributed to the evaporation of the $Ir(acac)_3$ precursor: its vaporisation temperature, between 200-250°C (as seen from thermogravimetric studies), is below its decomposition temperature at 250°C (Kemell et al., 2006; Walsh et al., 2009) in oxygen reactive gas and 370°C in argon atmosphere (Vargas Garcia et al., 2003). In literature, $Ir(acac)_3$ is reported as a suitable precursor for organometallic chemical vapour deposition (OMCVD) where the precursor first needs to evaporate to form a vapour, after which it undergoes decomposition on the target substrate (Vasilyev et al., 2015). However, in the presently used OMCD method, the vapour phase of the precursor is not required for the process, because the precursor is directly mixed with the support material. Instead, evaporation before decomposition of the precursor results in the transport of the precursor away from the support material, with subsequent deposition of an iridium film elsewhere, e.g. on the reactor walls. To minimize this iridium loss, it is envisaged that the design of the OMCD will be optimised, and other iridium precursors will be explored in the future.

In oxygen gas, the loading of iridium attained increased from 320-520°C, where a maximum Ir loading of 12 wt.% was obtained at 520°C. At 620°C, deposition in oxygen resulted in the lowest iridium loading attained in this environment, 6.4 wt.% Ir. In contrast to oxygen, synthesis in argon resulted in a steady decrease in iridium loading from 320-520°C. However, similarly to deposition

in oxygen, the lowest iridium loading in argon atmosphere was also attained at a temperature of 620°C. Interestingly, deposition at 720°C in argon resulted in the highest iridium loading in comparison to all the synthesis parameters that were explored.

### 6.2.2 Electrochemical Activity Screening

To quickly and accurately understand the electrochemical performance of the synthesised electrocatalysts in relation to the preparation conditions, the iridium-based mass-specific activity of the catalysts was determined at an applied potential of 1.525 V vs. RHE (***Figure 6-3***). Here, there are some general trends that are visible, relating the observed oxygen evolution mass-specific activity to the temperature and gas environment used for deposition, prior to the use of advanced physical characterisation techniques.

For the oxygen-synthesised catalyst materials, the mass-specific OER activity decreases as the synthesis temperature is increased. A possible explanation for this is that, as the temperature increases, the deposited $IrO_x$ particles experience particle growth, leading to a decrease in the electrocatalytically active surface area, causing a decline in mass-specific oxygen evolution activity. Elevated temperatures in the presence of oxygen are known to promote the development of crystalline iridium (IV) oxide phases (Geiger et al., 2016; Pfeifer, Jones, Vélez, et al., 2016) – as explained in the literature review, in the case of unsupported iridium oxides, crystalline, rutile phases are known to exhibit poor mass-specific OER activity in comparison to their amorphous counterparts. This could be another cause for the declining mass activity observed in the oxygen-synthesised $IrO_x$/ATO catalysts, as the deposition temperature was increased.

The relationship between temperature and the mass-specific OER activity observed in $IrO_x$/ATO catalysts prepared in argon seems to be much more complex than for catalysts which were prepared in oxygen. From 320-520°C a similar trend as catalysts prepared in oxygen is observed; the steady decline in mass activity is likely to be as a result of increased $IrO_x$ particle growth at elevated temperatures. It should however be noted that, at 320°C and 420°C, the mass-specific activity attained by the argon-prepared catalysts is consistently lower than that of the oxygen synthesised materials. Based on the reported works on Ir deposition using $Ir(acac)_3$ as a precursor (Locatelli et al., 2000; Nassreddine et al., 2010), deposition in argon would be expected to result in the formation of predominantly metallic iridium, whereas in oxygen, it would be expected that the most dominant phases from the deposition would consist of oxidised iridium. Metallic iridium is generally inactive towards oxygen evolution until it is electrochemically activated into an amorphous iridium oxide which can then efficiently catalyse the OER (Kötz, 1984; Reier, Oezaslan & Strasser, 2012; Saveleva et al., 2018). This would explain the lower mass-activity that is observed in argon-deposited catalysts, in comparison to those prepared in oxygen at 320°C and 420°C.

Interestingly, OMCD in argon at 620°C resulted in a mass-specific activity of 26 A $g^{-1}_{Ir}$, a result that is very similar to the synthesis at 320°C in argon which exhibited a mass-specific activity of 31 A $g^{-1}_{Ir}$ at 1.525 V vs. RHE. Deposition in argon at 720°C resulted in a fairly low mass-specific

OER activity of 6.4 A $g^{-1}_{Ir}$ – this could possibly be as a result of antimony segregation due to the extremely high reaction temperature. Strategies to optimise the iridium deposition yield achieved in the OMCD process are explored in Chapter 8. To truly understand the effect of gas environment and temperature on the mass-specific activity of the OMCD catalysts, further physical characterisation was required. Four catalysts were down selected for detailed, rigorous characterisation using high resolution scanning transmission electron microscopy to understand the morphology of the material, and X-ray photoelectron spectroscopy to understand the chemical state of the surface constituents.

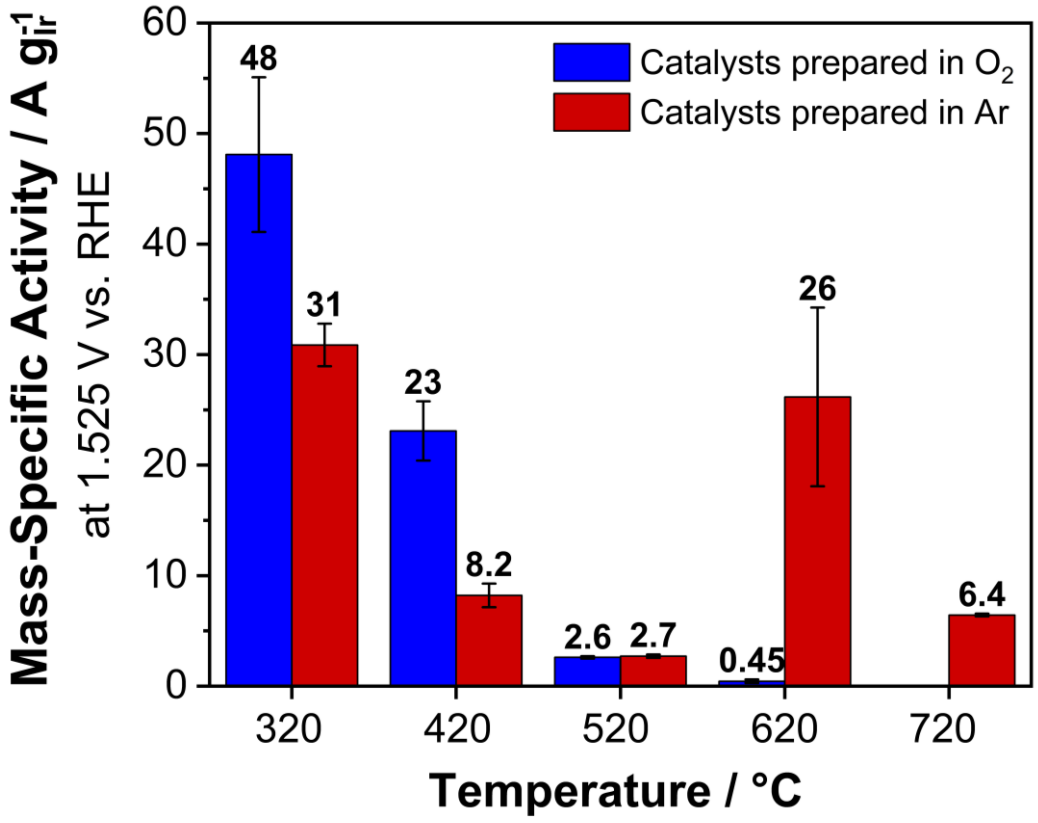


***Figure 6-3:*** *Electrochemical OER activity screening of OMCD $IrO_x$/ATO catalysts at an applied potential of 1.525 V vs. RHE.*

The catalysts selected were those synthesised at 320°C and 620°C in both oxygen and argon environments. For oxygen, these two temperature extremities were chosen in order to understand the reasons for which elevated temperatures result in a decline of mass-specific OER activity, and in the case of argon, catalysts prepared at 320°C and 620°C were chosen because of their unexpected similarity in OER mass-activity. Moreover, these selections would also allow for comparison of the effect of gas environment across the same temperatures.

## 6.3 DETAILED CHARCTERISATION

### 6.3.1 High Resolution Scanning Transmission Electron Microscopy (HR-STEM)

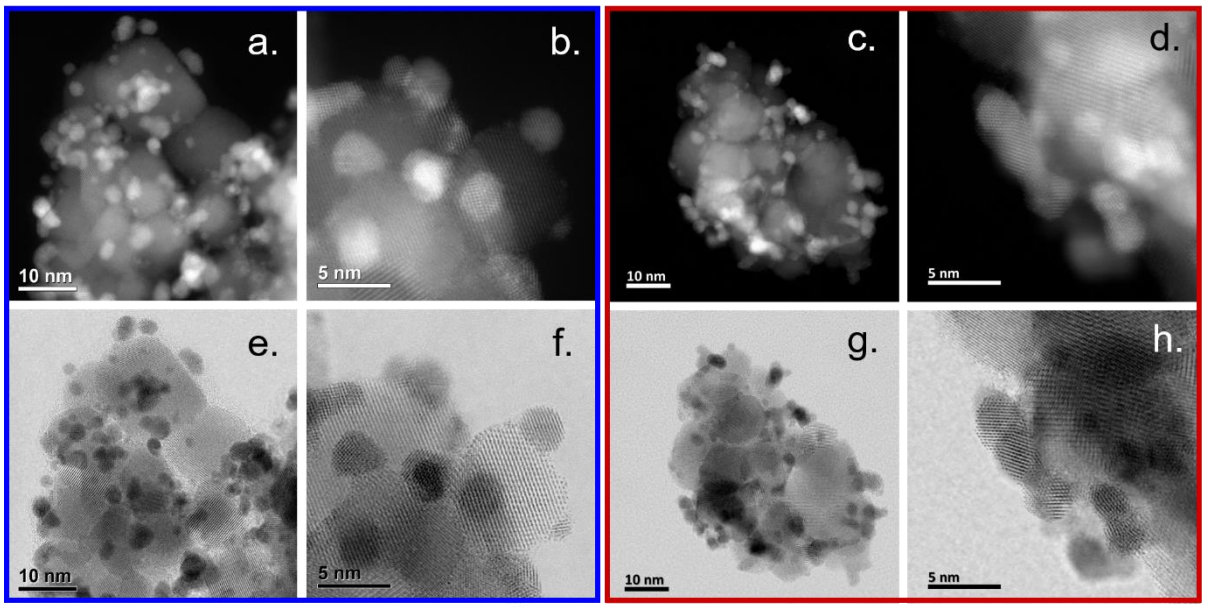


***Figure 6-4**: High-resolution scanning transmission electron microscopy (HR-STEM) images of OMCD $IrO_x$/ATO prepared in oxygen (9.4 wt.% Ir) and argon (11.4 wt.% Ir) at 320°C, where images (a-d) are high-angle annular dark field (HAADF) images and (e-h) are bright field images. The images in the blue box represent catalyst $O_2$-320°C, whereas the red box represents images from catalyst Ar-320°C.*

Representative images from HR-STEM of the as-synthesised $IrO_x$/ATO prepared in oxygen and argon at 320°C are shown above in ***Figure 6-4***. For catalyst $O_2$-320°C, highly dispersed $IrO_x$ nanoparticles were deposited, whereas in catalyst Ar-320°C, slightly more agglomerated particles were deposited onto the ATO support. An average $IrO_x$ particle diameter of 2.3 ± 0.7 nm was observed in $O_2$-320°C, and a larger average size of 3.4 ± 1.1 nm was achieved in catalyst Ar-320°C (see particle size distributions in ***Figure 6-5***) – these particle sizes are comparable to sizes of 1-5 nm that were achieved by traditional, wet chemistry deposition methods (Puthiyapura et al., 2014; Böhm et al., 2019; Solà-Hernández et al., 2019).

Careful analysis of the lattice spacings visible on the HR-STEM images for catalysts $O_2$-320°C and Ar-320°C confirmed the presence of rutile tetragonal $IrO_2$ nanoparticles, and the presence of some metallic Ir nanoparticles – see ***Table 6-1*** and ***Table 6-2*** below. While these results would be expected for synthesis in oxygen, the results are rather unexpected for treatment in argon, as this would be expected to result in mostly metallic iridium, as opposed to oxidised iridium.

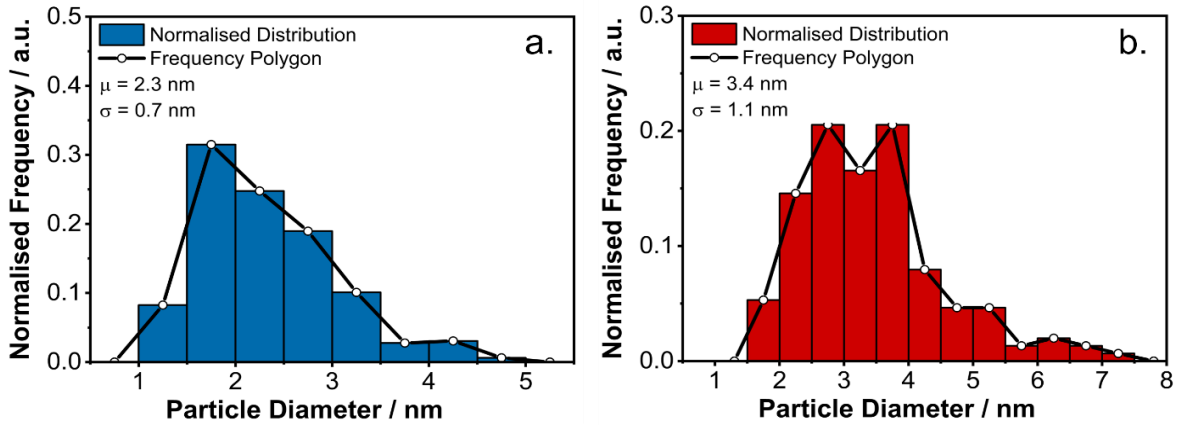


***Figure 6-5:*** *Particle size distributions of $IrO_x$ nanoparticles over the ATO support for catalyst $O_2$-320°C (a) and Ar-320°C (b) are shown.*

***Table 6-1:*** *Measured lattice spacings of $IrO_x$ from catalyst $O_2$-320°C with comparison to the closest $IrO_2$ and Ir metal spacing. This was performed on 7 $IrO_x$ particles (see* ***Figure B-1*** *in* ***Appendix B*** *for HR-STEM images of these particles).*

| Particle | Measured d-spacing / Å | Closest d-spacing in tetragonal $IrO_2$ / Å | Closest d-spacing in cubic Ir / Å | Most likely phase |
|---|---|---|---|---|
| 1 | 2.42 ± 0.06 | 2.58 (101) | 2.22 (111) | $IrO_2$ |
| 2 | 2.23 ± 0.02 | 2.25 (200) | 2.22 (111) | Ir |
| 3 | 2.41 ± 0.10 | 2.58 (101) | 2.22 (111) | $IrO_2$ |
| 4 | 2.18 ± 0.04 | 2.25 (200) | 2.22 (111) | Ir |
| 5 | 2.26 ± 0.02 | 2.25 (200) | 2.22 (111) | $IrO_2$ |
| 6 | 2.23 ± 0.12 | 2.25 (200) | 2.22 (111) | Ir |
| 7 | 2.58 ± 0.01 | 2.58 (101) | 2.22 (111) | $IrO_2$ |

***Table 6-2:*** *Measured lattice spacings of $IrO_x$ from catalyst Ar-320°C with comparison to the closest $IrO_2$ and Ir metal spacing. This was performed on 5 $IrO_x$ particles (see* ***Figure B-2*** *in* ***Appendix B*** *for HR-STEM images of these particles).*

| Particle | Measured d-spacing / Å | Closest d-spacing in tetragonal $IrO_2$ / Å | Closest d-spacing in cubic Ir / Å | Most likely phase |
|---|---|---|---|---|
| 1 | 2.43 ± 0.04 | 2.58 (101) | 2.22 (111) | $IrO_2$ |
| 2 | 2.41 ± 0.08 | 2.58 (101) | 2.22 (111) | $IrO_2$ |
| 3 | 2.12 ± 0.05 | 2.25 (200) | 2.22 (111) | Ir |
| 4 | 2.29 ± 0.03 | 2.25 (200) | 2.22 (111) | $IrO_2$ |
| 5 | 2.18 ± 0.06 | 2.25 (200) | 2.22 (111) | Ir |

The distribution of Sn, Sb and Ir components for catalysts $O_2$-320°C and Ar-320°C, determined by EDX elemental mapping is seen in ***Figure 6-6***: it is seen that in both catalysts, the tin signal is distributed uniformly across what is identified as the support material. The Ir signals are clustered, and it is evident from the colour composite image that they are coming from well distinguishable $IrO_x$ nanoparticles distributed across the ATO support, further confirming the successful preparation of a supported catalyst. There are however differences concerning the two catalysts that are visible from the distribution of the Ir signal; the catalyst prepared in argon seems to have more agglomeration than the catalyst which was prepared in oxygen. These differences are clearly visible in the EDX maps in ***Figure 6-6***, where in ***Figure 6-6(d)*** (the catalyst prepared in oxygen at 320°C) the iridium signal is more evenly distributed than the signal in ***Figure 6-6(h)*** (preparation in argon at 320°C), where the iridium signal is more densely and unevenly distributed over the ATO support.

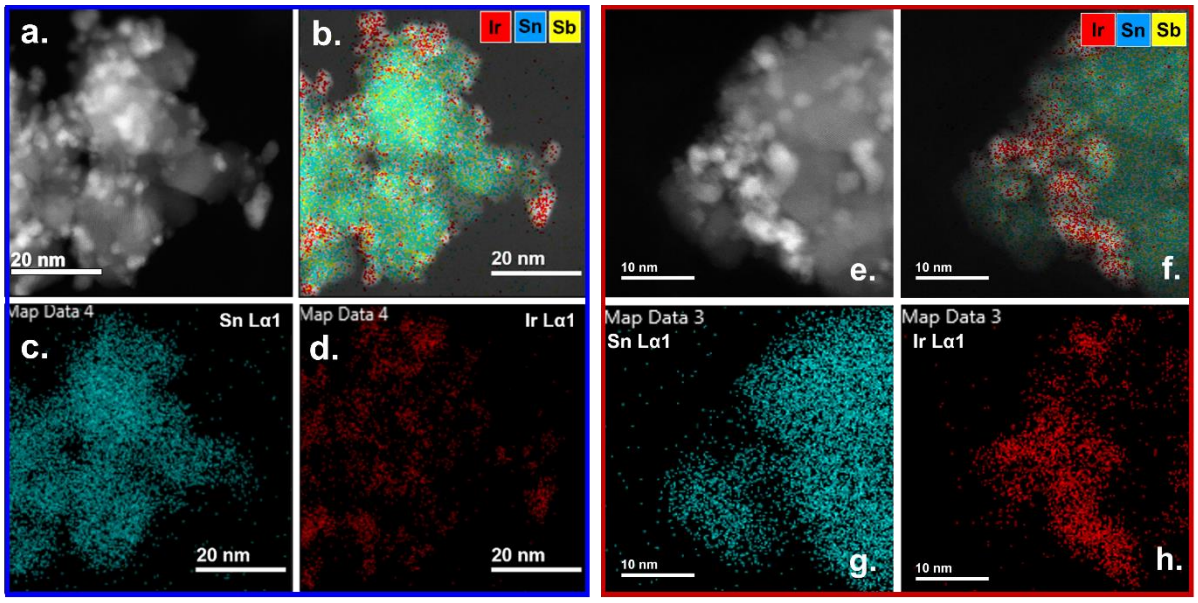


***Figure 6-6:*** *HR-STEM EDX maps: HAADF images for OMCD $IrO_x$/ATO (a and e), colour composite elemental maps (b and f), Sn signal distribution (c and g) and Ir signal distribution (d and h). The images and maps in the blue box represent catalyst $O_2$-320°C, whereas the red box represents catalyst Ar-320°C.*

Representative images from HR-STEM of the as-synthesised $IrO_x$/ATO prepared in oxygen and argon at 620°C are shown below in ***Figure 6-7***. Catalyst $O_2$-620°C barely shows any signs of deposited iridium particles, however, the catalyst prepared in argon at 620°C shows the presence of what seems to be $IrO_x$ clusters. In both cases, it was not possible to plot particle size distributions, as a very few number of particles could be found in catalyst Ar-620°C, and in catalyst $O_2$-620°C, there were virtually no visible $IrO_x$ particles.

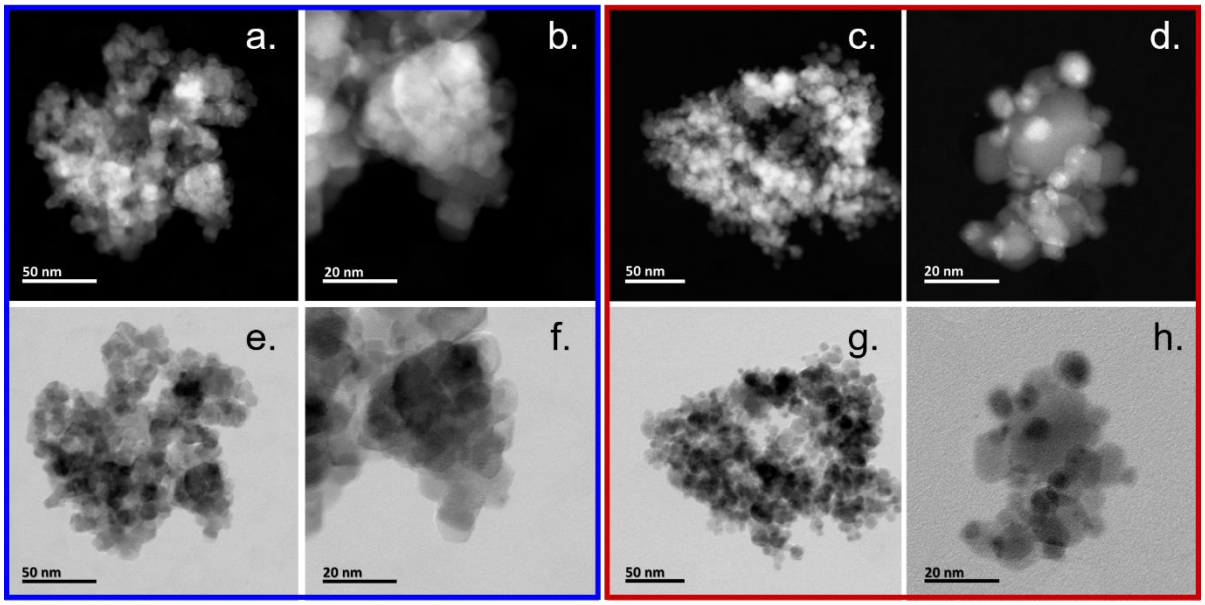


***Figure 6-7:*** *High-resolution scanning transmission electron microscopy (HR-STEM) images of OMCD $IrO_x$/ATO prepared in oxygen (6.4 wt.% Ir) and argon (4.2 wt.% Ir) at 620°C, where images (a-d) are high-angle annular dark field (HAADF) images and (e-h) are bright field images. The images in the blue box represent catalyst $O_2$-620°C, whereas the red box represents images from catalyst Ar-620°C.*

The distribution of Sn, Sb and Ir components for catalysts $O_2$-620°C and Ar-620°C, determined by EDX elemental mapping is seen in ***Figure 6-8.*** While in both cases the presence of a supported catalyst is confirmed, catalyst $O_2$-620°C has a stronger Ir signal than in Ar-620°C, relative to the Sn signals.

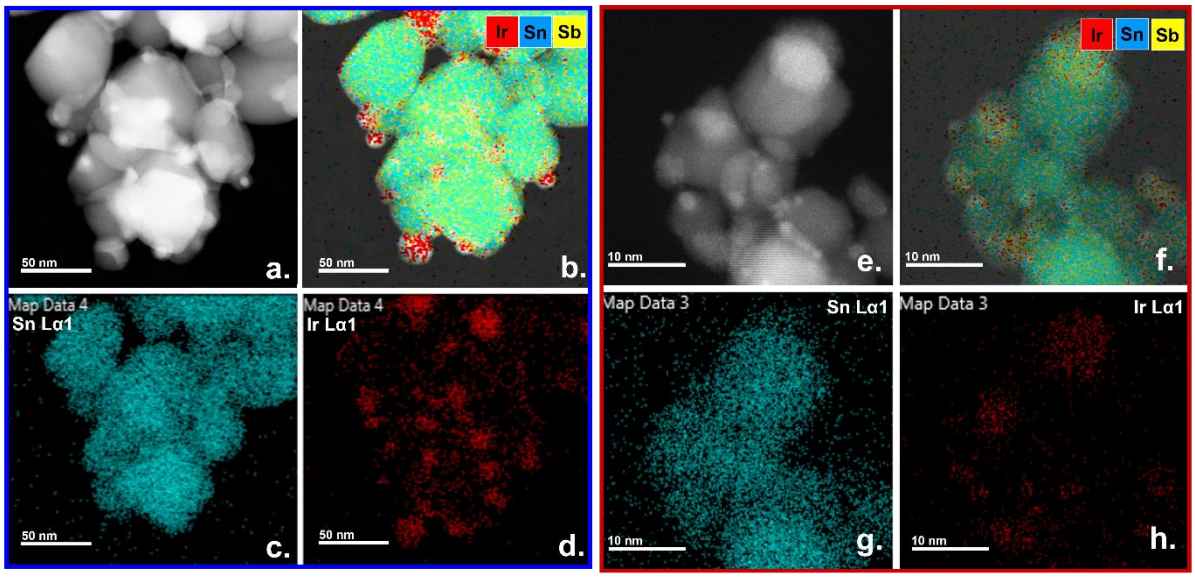


***Figure 6-8:*** *HR-STEM EDX maps: HAADF images for OMCD $IrO_x$/ATO (a and e), colour composite elemental maps (b and f), Sn signal distribution (c and g) and Ir signal distribution (d and h). The images and maps in the blue box represent catalyst $O_2$-620°C, whereas the red box represents catalyst Ar-620°C.*

### 6.3.2 X-ray Diffraction (XRD)

Structural characterisation of the synthesised materials was performed using X-ray diffraction - see ***Figure 6-9*** below. While no distinguishable features of iridium oxide or metallic iridium were observed at synthesis at 320°C, some metallic iridium features were seen in catalyst Ar-620°C. The lack of distinguishable features in the other catalysts is likely to be as a result of low iridium loadings, small particle sizes or masking of the iridium oxide reflexes by the $SnO_2$ pattern.

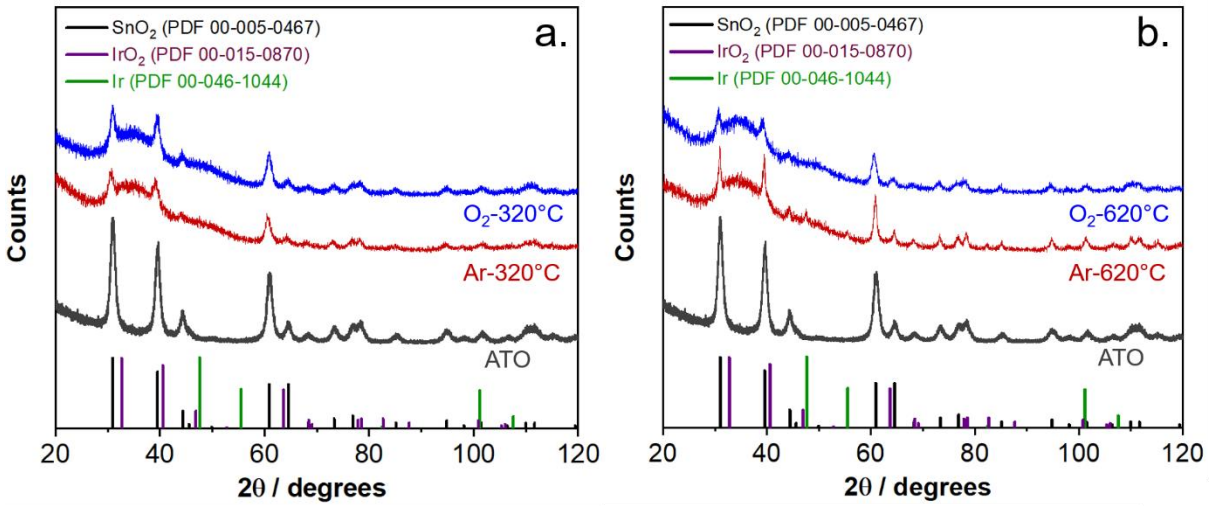


***Figure 6-9**: X-ray diffraction for OMCD $IrO_x$/ATO catalysts which were prepared in oxygen and argon at 320°C (a) and 620°C (b), measured using a Co-$K_a$ radiation source.*

### 6.3.3 X-ray Photoelectron Spectroscopy (XPS)

To further understand the organometallic deposition method, it was necessary to perform X-ray photoelectron spectroscopy measurements on the four catalysts which were selected for rigorous characterisation, in order to gain a further understanding towards the chemical species which were present on the surfaces of these materials. The discussion for the XPS portion of this chapter is explained in two ways: the first is a discussion around the raw data from the narrow scans, and the second is a detailed explanation of the iridium and oxygen components present in the Ir 4f and O 1s spectra across all four catalysts, based on results from curve fitting. The analysis of the raw XPS data in the narrow scans is quite a useful way to discern differences across the synthesised materials without necessarily doing any curve fitting, and in the case of this work, some interesting conclusions can be drawn upon an examination of the features in these scans, before referring to any curve fitted results. The narrow scans for the C 1s, Sb 3d, O 1s, Ir 4f, Sn 3d and Ir 4p regions are discussed. Curve fitting of the Ir 4f and O 1s spectra was performed to elucidate the oxidation state of the iridium, and determine the nature of the oxygen containing components on the surface of the synthesised materials. As explained in the literature review, the chemical state of iridium and the nature of the iridium oxide phase (amorphous or crystalline) have a major influence on the performance of iridium-based catalytic materials.

### *6.3.3.1 Analysis of the Raw Data*

The discussion for this section is based on ***Figure 6-10*** below.

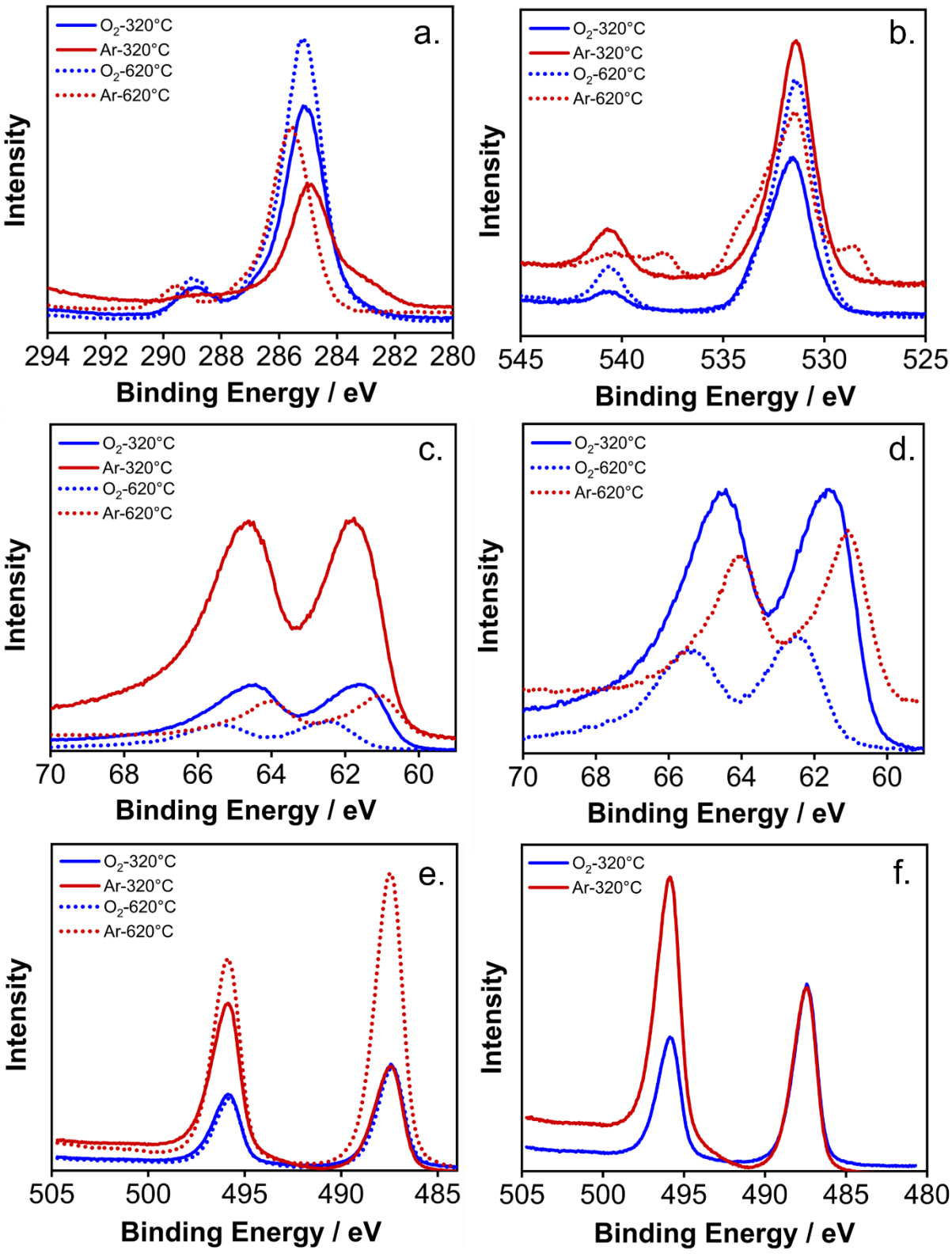


***Figure 6-10****: XPS raw data. Narrow scans showing the C 1s region (a), the Sb 3d and O 1s regions (b), the Ir 4f region (c-d), and the Sn 3d and Ir 4p regions (e-f).*

Interestingly, the peak corresponding to adventitious carbon in the OMCD $IrO_x$/ATO catalyst that was prepared in argon at 620°C appears to have a slight shift of 0.4 eV towards higher binding energies. XPS measurements can be expected to have a small degree of instrument related error, usually in the range of 0.1-0.2 eV. In this context, the slight shift seen in the carbon 1s spectrum for the catalyst prepared in argon at 620°C is approximately 0.2 eV towards higher binding energies, after the inclusion of error; while this shift would suggest a small degree of charging during the XPS measurement of this catalyst, it is a very minor shift and therefore no energy correction was used on the binding energy scale.

Asides from the understanding of whether or not there is sample charging, further information pertaining to the OMCD method can be extracted from the C 1s spectra in ***Figure 6-10(a)***. Both catalysts prepared in oxygen, as well the catalyst that was prepared in argon at 620°C seem to contain similar carbon species on their surfaces. However, the catalyst prepared in argon at 320°C contains different features than the other three materials; there is no contribution between 288-290 eV as there is in the other materials, and notably, this catalyst also has a shoulder-like feature from 282-284 eV. This feature may suggest the formation of carbide species in argon at 320°C that are absent in catalysts prepared in the other synthesis conditions.

The narrow scan in the binding energy region for Sb 3d and O1s is shown in ***Figure 6-10(b).*** Here, it is immediately clear that OMCD in argon at 620°C results in different oxygen and antimony containing species than those in the other three synthesis conditions. All syntheses in oxygen, as well as synthesis at 320°C in argon exhibit a peak at a binding energy of 540.43 eV, which is characteristic of $Sb^{5+}$. It is challenging to confirm the presence of $Sb^{3+}$ (and therefore $Sb_2O_3$) without curve fitting, as a result of this component overlapping with the O 1s peak that occurs between 535-528 eV. The catalyst which was synthesised at 620°C in argon contains two additional features which are not visible in the spectra of the other three materials: there are visible peaks corresponding to 528.35 eV and 538.0 eV on either side of the O 1s spectrum, confirming the presence of metallic antimony, $Sb^0$. This result suggests that high temperature deposition in argon atmosphere results in segregation of antimony from the ATO support.

The Ir 4f spectra, seen in ***Figure 6-10(c-d)***, provides some interesting insights towards the nature of iridium species that are present on the surface of the synthesised materials. In ***Figure 6-10(c)***, the most noticeable feature is the higher intensity of the Ir 4f signal in the catalyst that was prepared at 320°C in argon, in comparison to the materials prepared in the other three synthesis conditions. While it is not possible to draw quantitative conclusions pertaining to the Ir loading in the catalysts from these varying intensities in the Ir 4f signal, it can be qualitatively concluded that the iridium loading in the OMCD $IrO_x$/ATO catalyst prepared in argon at 320°C had the highest iridium loading, compared to catalysts prepared in oxygen at 320°C and 620°C, and argon at 620°C. Analysis of the narrow scan in the Ir 4p and Sn 3d region further confirms this conclusion. In ***Figure 6-10(e-f)***, all the peaks that are visible are from the Sn 3d doublet (Sn $3d_{5/2}$ and Sn $3d_{3/2}$ at 487.30 eV and 495.0 eV, respectively); the Ir $4p_{3/2}$ peak which also occurs at a binding energy of

495.0 eV is masked entirely by the Sn 3d peak at the same binding energy. This is evident in the fact that across catalysts $O_2$-320°C, $O_2$-620°C and Ar-620°C, the intensity ratio between the Sn 3d peaks is maintained, with the exception of catalyst Ar-320°C, where this intensity ratio of these two Sn 3d peaks is inverted. The Ir 4f spectra in ***Figure 6-10(c-d)*** clearly shows that catalyst Ar-320°C exhibits the highest peak intensity, and as Ir 4f is generally the characteristic, most intense peak for the XPS spectrum of iridium, if this peak has an exceptionally high intensity, the Ir $4p_{3/2}$ peak for the same material will also have a higher contribution than in catalysts which contain a lower Ir 4f peak intensity. Therefore, the inverted appearance of the intensity ratio of the Sn 3d peaks in catalyst Ar-320°C that is observed in ***Figure 6-10(e)***, is likely to be as a result of a higher Ir $4p_{3/2}$ signal at 495.0 eV, as this catalyst contains the highest iridium loading across the four catalysts. This analysis is well-supported by the EDX analysis which showed that compared to catalysts $O_2$-320°C (9.4 wt% Ir), $O_2$-620°C (6.4 wt.% Ir), and Ar-620°C (4.2 wt.% Ir), catalyst Ar-320°C contained the greatest content of iridium (11 wt.% Ir).

By this logic, at first glance of the Ir 4f spectra in ***Figure 6-10(c-d)***, it seems peculiar that the catalyst prepared in oxygen at 620°C (6.4 wt.% Ir) should have a lower peak intensity than that of the catalyst prepared in Ar at 620°C, which exhibits a higher Ir 4f peak intensity, and a lower iridium mass loading of 4.2 wt. %. However, in XPS measurements, ejected photoelectrons can only escape a depth of 2-5 nm of the sample surface (Niemantsverdriet, 2007; Che & Védrine, 2012), and the catalyst prepared in oxygen at 620°C contains the largest carbon contribution, compared to the catalysts prepared in the other preparation conditions. This could have resulted in attenuation/suppression of the iridium signal in this particular catalyst, as a result of a large presence of carbon containing compounds on the surface, preventing the escape of some of the photoelectrons from deeper depths in the material which would have contributed towards the iridium signal.

The position of the peaks in the raw data from the Ir 4f spectra ***Figure 6-10(c-d)*** provide a preliminary indication of the most dominant iridium phase present in the different catalysts. Iridium is peculiar in that there is a reverse binding energy shift for $Ir^{4+}$ and $Ir^{3+}$; peaks attributed to higher oxidation states usually occur at higher binding energies, however, in the case of iridium, $Ir^{3+}$ exhibits a higher binding energy (at 62.4 eV) than $Ir^{4+}$, with a contribution at 61.5 eV (Pfeifer, Jones, Vélez, et al., 2016). In addition, if metallic iridium is present, a contribution can be expected at a binding energy of 60.8 eV. While a detailed analysis of the Ir 4f components present in the four catalysts will be explained in the following section, the information mentioned above is sufficient to allow for some general conclusions to be drawn, pertaining to the most likely dominant Ir species present in these catalysts. The Ir 4f spectrum for catalyst Ar-620°C is shifted to a lower binding energy than any of the other catalysts, suggesting that this catalyst contains the greatest presence of metallic iridium, compared to the other materials. This finding is rather fascinating; considering that the analysis of the Sb 3d region of this catalyst contained metallic antimony, it seems probable that in this reaction environment, organic products from the

decomposition of the iridium acetylacetonate precursor act as reducing agents, promoting the deposition of metallic iridium, but also antimony segregation from the ATO support. On the other hand, the catalyst prepared at 620°C in oxygen seems to have a strong presence of $Ir^{3+}$, with peak contributions at higher binding energies than those observed for the other catalysts. The two catalysts prepared at 320°C in oxygen and argon environments interestingly seem to have $Ir^{4+}$ as the dominating Ir species on their surfaces – while it is highly possible for iridium (IV) oxide to have formed during deposition at 320°C in oxygen, it is unexpected that the same would have occurred at 320°C in argon, owing to the fact that here, there is hardly any oxygen available for reaction, asides from oxygen in the $Ir(acac)_3$ precursor and the ATO support.

#### *6.3.3.2 Analysis of Components in the Ir 4f and O 1s Spectra*

While some firm and insightful discoveries pertaining to the four down selected OMCD $IrO_x$/ATO catalysts were made by analysis of the raw XPS data, quantitative information can only be drawn by curve fitting of the XPS spectra. The Ir 4f and O 1s spectra of the catalysts were curve fit using similar approaches to Pfeifer, Jones, Vélez, et al. (2016) and Yu et al. (2018). The quantification of the various components in the Ir 4f and O 1s spectra are summarised in ***Figure 6-11*** below, where the contribution of each component was determined based on the fitted area of each component, relative to the total fitted area. For the curve-fitted spectra, please refer to ***Figure 6-12(a-h)***.

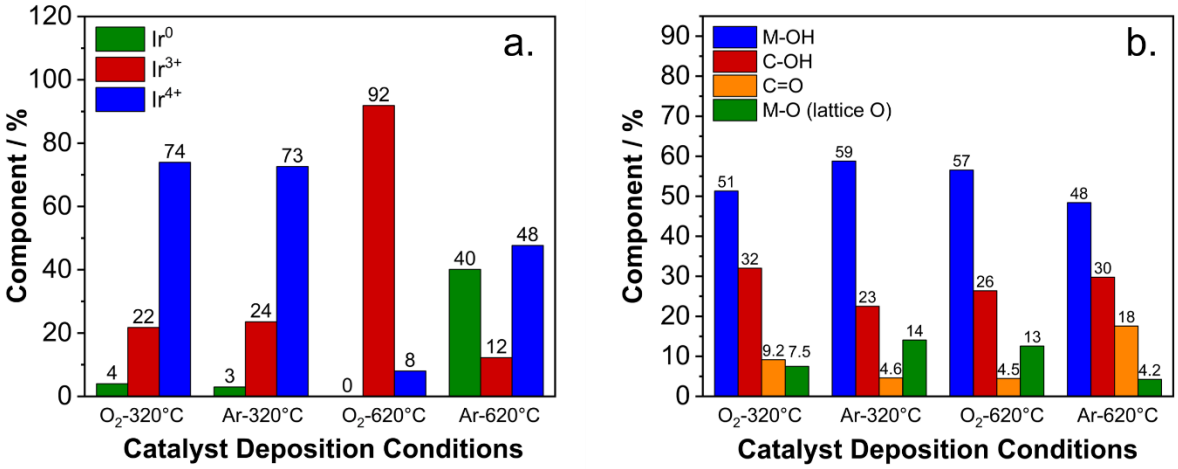


***Figure 6-11:*** *Component contributions for Ir 4f (a) and O 1s (b) for OMCD $IrO_x$/ATO catalysts prepared at 320°C and 620°C, in oxygen and argon atmospheres.*

Curve fitting for the O 1s and Ir 4f spectra is seen in ***Figure 6-12***. As seen in ***Figure 6-11*** above, analysis of the fitted Ir 4f spectrum for the catalyst prepared at 320°C in oxygen (***Figure 6-12(a)***) proved that $Ir^{4+}$ was the dominant Ir species, with a contribution of 74% at 61.5 eV. The remainder of the spectrum contains 22% $Ir^{3+}$ at 62.4 eV and a small contribution from metallic iridium species (4%) at a binding energy of 60.8 eV. These results are in qualitative agreement with HR-STEM, where both rutile iridium (IV) oxide and iridium metal were observed. This implies that while the

OMCD deposition technique was successful in directly depositing crystalline $IrO_2$ nanoparticles on the ATO support, in a one-step process, there is a small proportion of metallic iridium particles which do not undergo complete oxidation. From the O 1s spectrum (***Figure 6-12(b)***), it can be concluded that the surface of the catalyst was hydrated. However, the corresponding and most dominant peak at a binding energy of 531.5 eV presumably contains a contribution from both hydrated Ir, Sn and Sb oxides, so that it is not possible to distinguish between surface hydroxylation of the ATO support versus the iridium oxide. Peaks at higher binding energies are assigned to oxygen components arising from hydrocarbon species present at the surface of the catalyst. This is in agreement with the components detected from the C 1s signal: C-O at 286.3 eV and O-C=O at 288.8 eV, while aliphatic carbon was at 285.0 eV. The presence of hydrocarbon components is likely result of the incomplete hydrocarbon removal during $Ir(acac)_3$ decomposition, which potentially also acts as a surfactant and reducing agent for iridium-containing phases during the deposition process.

Interestingly, the contributions from the components in the Ir 4f spectrum for the catalyst prepared in argon at 320°C were almost identical to those observed in the catalyst which was prepared at the same temperature in oxygen. The similarity of the results across these two catalysts is difficult to comprehend: decomposition of $Ir(acac)_3$ in oxygen at 300°C is known to form iridium oxide, however, decomposition in a neutral atmosphere, such as argon, is expected to result in the formation of predominantly metallic iridium species (Vargas Garcia et al., 2003; Nassreddine et al., 2010). The results for the quantification of the Ir 4f spectra in the catalyst prepared at 320°C in oxygen are therefore plausible, however, the results for the catalyst prepared in argon at the same temperature cannot be justified. The almost identical nature of the acquired Ir spectra for the two catalysts would strongly suggest that the deposition, which was seemingly performed under an argon atmosphere, had a presence of oxygen gas in the reaction chamber. It is not clear whether this oxygen came from a leak in the reaction system, a presence of oxygen in the argon delivery line to the reactor, or an unintentional, direct delivery of oxygen to the reactor tube instead of argon. Furthermore, it is unlikely that oxygen from the (acac)-ligands was incorporated into the Ar-320° catalyst, as the known products for $Ir(acac)_3$ decomposition in argon are $H_2$, CO, $CO_2$ and $CH_4$ (Nassreddine et al., 2010). While the catalyst prepared in argon at 320°C has similar Ir 4f component contributions to catalyst in comparison to catalyst $O_2$-320°C, the results from HR-STEM illustrated that a larger average $IrO_x$ particle size (3.4 ± 1.1 nm) was achieved, and lattice spacing analysis confirmed the presence of rutile iridium (IV) oxide, supporting the results obtained in the analysis of the Ir 4f spectra.

The quantification of the O 1s spectra for the two catalysts prepared at 320°C exhibit more distinct differences than the similarities which were observed in the iridium 4f spectra of the same. Here, the catalyst prepared in argon has a lower proportion of C-OH and C=O components, but, an almost 2-fold larger contribution from metal bonded to lattice oxygen than that which was observed in the $O_2$-320°C catalyst. Notably, the analysis of the C 1s spectra illustrated that the carbon species across these two catalysts was rather different, where the catalyst prepared in argon

at 320°C showed the possibility of carbide species. While there are differences in particle morphology, carbon and oxygen containing species on the surface of catalyst Ar-320°C, the almost identical component proportions of the Ir 4f spectra in comparison to the catalyst prepared at the same temperature in oxygen leave some questions behind about the integrity of the synthesis of catalyst Ar-320°C. It seems that the best way to understand this synthesis will be to repeat it and to examine whether or not the same results will be achieved.

Quantification of the Ir 4f spectrum of the catalyst prepared in oxygen at 620°C showed that the dominating Ir species was $Ir^{3+}$ (with a 92% contribution), where the remaining contribution comes from $Ir^{4+}$. At first glance, it is counter-intuitive that in deposition in $O_2$ at 320°C, the dominating iridium species is $Ir^{4+}$, but at 620°C there is mostly $Ir^{3+}$present; intuitively, one would expect oxidation to proceed more efficiently at higher temperatures. However, this intuition can be misleading. In fact, it only takes into account the kinetic point of view, where the oxidation kinetics are, of course, faster at higher temperatures. However, the opposite is true from the perspective of fundamental thermodynamics: thermodynamically, at higher temperatures the reduced phases of a metal are preferred. The reason for this is that higher temperatures favour the higher entropy state, and in this case, this corresponds to gas phase oxygen. Therefore, typically metal oxides release oxygen and become reduced even to metal at very high temperatures, because the lattice oxygen prefers to go to the high entropy oxygen gas phase compared to the low entropy crystal lattice (Asadian, 2012).

The observation of a dominating contribution from $Ir^{3+}$ in deposition in oxygen at 620°C can therefore be explained by the following: at higher temperatures, the formation of oxygen vacancies in the $IrO_2$ lattice becomes more favourable. Oxygen vacancy formation is preferred for entropic reasons at higher temperatures and it results in reduced $Ir^{3+}$ oxidation state. The same argument also explains why in argon atmosphere at 620°C, it is seen that we get metallic iridium (and segregated metallic Sb): again the oxygen poor phase is preferred at high temperatures and at very low oxygen partial pressure (in argon) the synthesis proceeds directly to metallic iridium.

The catalyst prepared in argon at 620°C contained the greatest contribution from metallic iridium compared to the other catalysts, in alignment with the analysis of the XPS raw data. Quantification of the Ir 4f spectrum for this catalyst showed that metallic iridium had a contribution of 40%, with a 48% contribution from $Ir^{4+}$, and the balance from $Ir^{3+}$ (12%). Nassreddine et al. (2010) studied the decomposition of $Ir(acac)_3$ in argon for catalysis applications. Here, they discovered that this precursor decomposes very slowly above 360°C in a pure argon atmosphere, with the dominating decomposition products from the ligand chains being $H_2$ (from 360°C), $CH_4$ (between 280-430°C), CO (at 425°C) and $CO_2$ (450-560°C). It was also noted in this study, that by 600°C the precursor had not fully decomposed. Analysis of the O 1s components for this catalyst shows the highest proportion of C=O than that seen in the other catalyst preparation environments, suggesting a different mode of precursor decomposition than in the other reaction conditions.

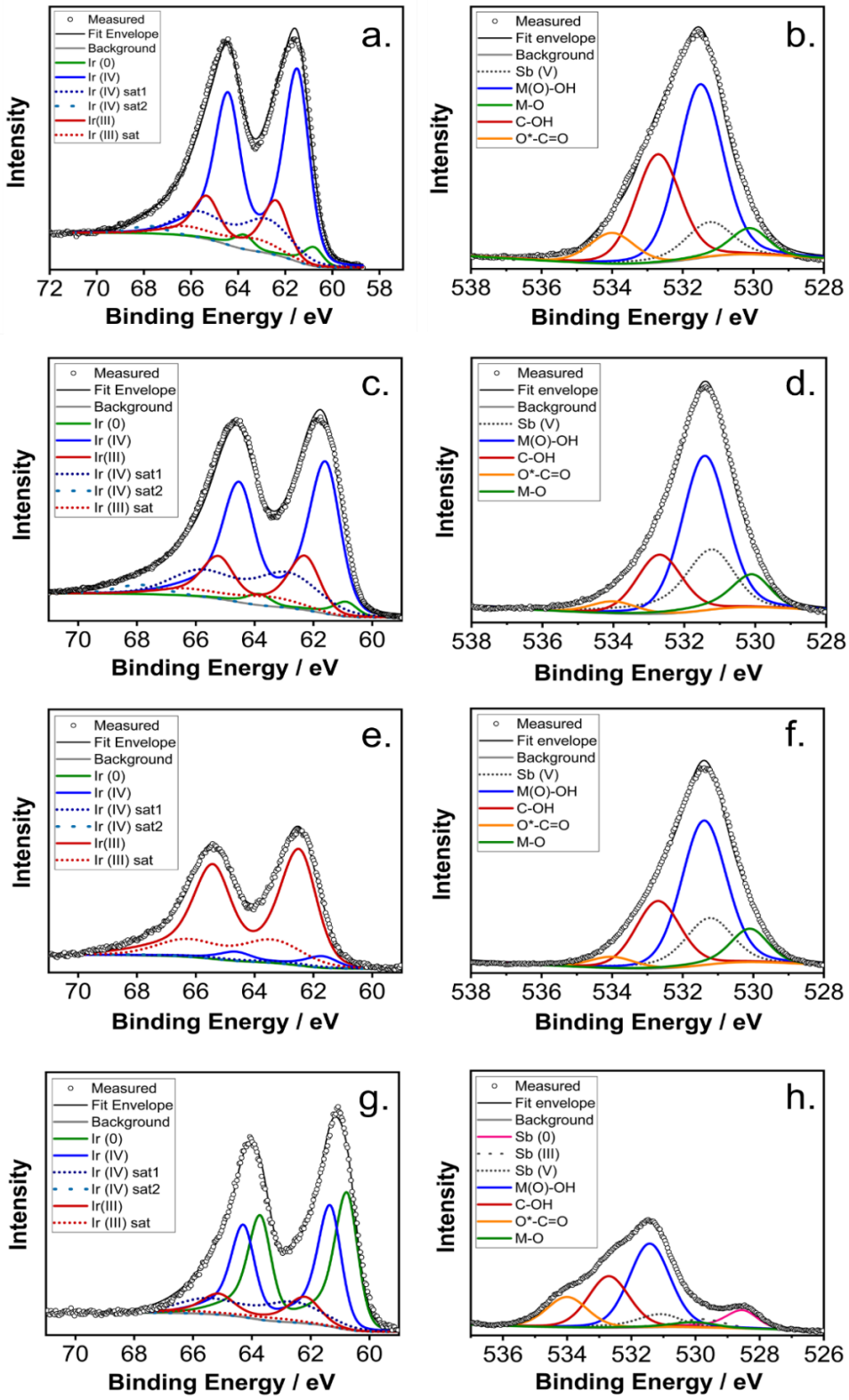


***Figure 6-12**: Curve-Fitted XPS spectra for Ir 4f and O 1s for OMCD $IrO_x$/ATO catalysts prepared in oxygen at 320°C (a-b), argon at 320°C (c-d), oxygen at 620°C (e-f) and argon at 620°C (g-h). All Ir 4f*

*spectra are fitted with curves for $Ir^0$, $Ir^{3+}$ and $Ir^{4+}$ components. The O 1s spectra are fitted with curves for various oxygen containing species, where 'M' denotes the metals Sn, Sb and Ir.*

As mentioned earlier, the O 1s spectra contain some overlapping contributions from Sb 3d components. ***Table 6-3*** below summarises the contributions of the Sb 3d spectra for the four catalyst preparation conditions.

| Sb 3d Component / % | $O_2$-320°C | Ar-320°C | $O_2$-620°C | Ar-620°C |
|---|---|---|---|---|
| $Sb^0$ | 0 | 0 | 0 | 39 |
| $Sb^{3+}$ | 0 | 0 | 0 | 24 |
| $Sb^{5+}$ | 100 | 100 | 100 | 37 |

***Table 6-3:*** *A summary of the contributions from the Sb 3d spectra for preparation of catalysts in oxygen and argon at 320°Cand 620°C.*

Here, it is seen that all the catalysts prepared in oxygen, as well as the catalyst which was prepared in argon at 320°C contain $Sb^{5+}$ on their surfaces; as Sb-doped $SnO_2$ is an n-type semiconductor, it is to be expected that Sb should be present in the material in 5+ state. These results would prove that the support is unaffected in these particular synthesis conditions. However, synthesis in argon at 620°C results in $Sb^0$ and $Sb^{3+}$ contributions, in addition to the presence of $Sb^{5+}$. In fact, the largest contribution in the Sb 3d spectrum of this catalyst comes from metallic antimony (39%), and this together with the contribution of $Sb^{3+}$ is likely to arise from the presence of reducing agents CO and $H_2$ in the reaction mixture, as well as from the fact that in high temperatures and low oxygen partial pressures, the formation of metallic states are preferred over formation of oxidised ones. Based on this analysis, together with the previous analysis of the Sn 3d spectra from the raw XPS data, it can be concluded that deposition of $IrO_x$ on ATO in argon at 620°C results in altering of the ATO support, and that these synthesis conditions are therefore not suitable for use with ATO support – Sb segregation will certainly diminish the electrical conductivity of the ATO support, given that in ATO, $SnO_2$ is doped with $Sb^{5+}$ for the sole purpose of inducing n-type electrical conductivity.

### 6.3.4 Electrochemical Performance Evaluation

Based on the rigorous physical characterisation that was performed on $IrO_x$/ATO catalysts that were prepared by organometallic chemical deposition in oxygen and argon environments at 320°C and 620°C, it was decided to perform further electrochemical characterisation on catalysts that were prepared in 320°C to understand the stability of these materials, in *ex-situ* OER reaction conditions. This decision was made because both of these materials exhibited reasonably high OER mass-activity during the initial screening measurements, which were performed at an applied

potential of 1.525 V vs. RHE. Furthermore, synthesis in oxygen at 620°C resulted in poor mass-activity, as a result of the presence of iridium sub-oxides which likely dissolved in the perchloric acid electrolyte, and deposition at the same temperature in argon caused antimony segregation, a phenomena which would have had detrimental consequences on the electronic conductivity of the ATO support.

Prior to physical characterisation, it was thought that the central reason behind the difference of mass-activity across synthesis in oxygen and argon at 320°C would be due to different iridium species present in the two catalysts. The material synthesised in argon was thought to contain mostly metallic iridium, based on the lack of oxygen that would be expected in an inert reaction environment; the catalyst prepared in oxygen was thought to contain predominantly iridium oxide species, an expectation based on literature findings (Locatelli et al., 2000; Nassreddine et al., 2010). Upon examination of these catalysts with physical characterisation techniques, it was discovered that in fact, the two materials contained almost identical proportions of $Ir^0$, $Ir^{3+}$ and $Ir^{4+}$ on their surfaces, but that the $IrO_x$ particle size achieved in argon was larger (3.4 ± 1.1 nm) in contrast to the smaller size achieved in the catalyst synthesised in oxygen (2.7 ± 0.7 nm).

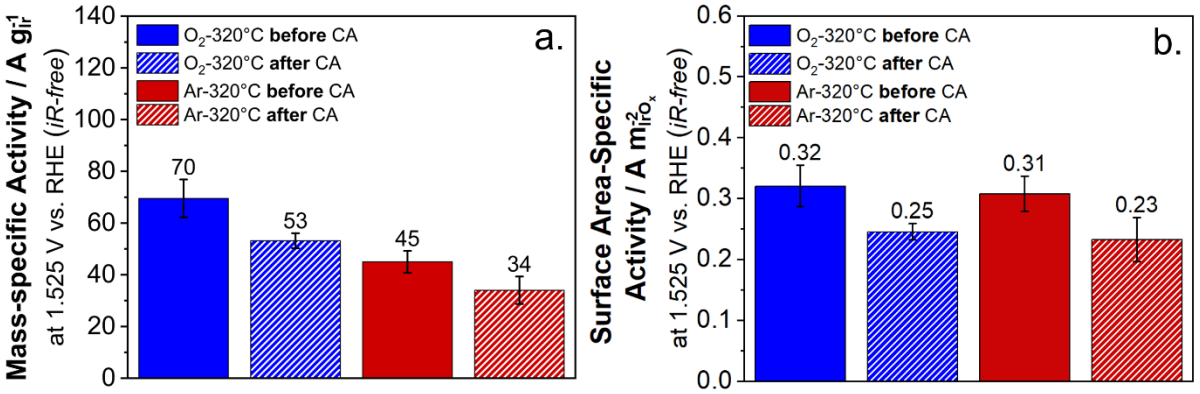


***Figure 6-13:*** *Oxygen evolution mass-specific activity (a) and surface area-specific activity (b) of $IrO_x$/ATO prepared in argon and oxygen at 320°C, at 1.525 V vs. RHE (iR-free) before and after chronoamperometry at 1.600 V vs. RHE (CA), for a period of two hours.*

***Figure 6-13*** above illustrates the mass-specific oxygen evolution activity of the catalysts which were prepared at 320°C in both oxygen and argon environments. It should be noted, that these results are reported at 1.525 V vs. RHE, *iR-free*, as opposed to the results in ***Figure 6-3***, where the mass-activities were reported at an applied potential of 1.525 V vs. RHE. This is the reason for why the mass-activities in ***Figure 6-13*** are larger than those reported in ***Figure 6-3***. As already seen in the OER screening section of this chapter, the catalyst prepared in oxygen exhibits an approximately 36% greater mass-specific OER activity, than that of catalyst Ar-320°C. As the two materials have the same starting iridium oxidation states, it is highly probable that the difference in mass-specific activity between the two catalysts is a result of difference in surface areas, a consequence of the larger particle sizes in Ar-320°C, as opposed to the smaller sizes achieved in $O_2$-320°C. After a potential hold at 1.6 V vs. RHE for a period of two hours, it was seen that the

two catalysts achieved the same relative loss of mass-activity of ~25%. One of the primary modes of deactivation in iridium oxide OER catalysts is the dissolution of iridium. This phenomena is strongly controlled by the oxidation state of the iridium in the catalysts. $Ir^{4+}$ is considered to be the most stable iridium phase, with $Ir^{3+}$ the most likely to undergo dissolution in iridium oxide materials (Cherevko et al., 2016; Pfeifer, Jones, Vélez, et al., 2016). Therefore, a possible explanation for the similar losses of mass-activity observed across the two catalysts is in the fact that both materials contain almost identical contributions from metallic iridium, as well as from $Ir^{3+}$ and $Ir^{4+}$. The geometric surface area of the deposited $IrO_x$ particles was calculated and utilised to convert the mass-specific OER activity of catalysts $O_2$-320°C and Ar-320°C in ***Figure 6-13(a)*** to specific activities on the basis of the surface area of the deposited $IrO_x$ particles, as seen in ***Figure 6-13(b)***. Further details on the calculations which were carried out to convert particle sizes obtined from HR-STEM measurements into geometric surface area can be found in ***Appendix C***. ***Figure 6-13(b)*** demonstrates that once normalised by surface area, the OER performances of catalysts $O_2$-320°C and Ar-320°C are in fact very similar, verifying that the lower mass-specific activity of catalyst Ar-320°C both before and after stability evaluation is due to the larger average $IrO_x$ particle size (3.4 nm) in this catalyst as opposed to the smaller size (2.3 nm) achieved in catalyst $O_2$-320°C.

# Chapter 7: An Outstanding OER Catalyst

*From the previous chapter, it was seen that the organometallic chemical deposition method using the decomposition of Ir(acac)$_3$ was indeed successful as a method to prepare iridium oxide supported on ATO. Synthesis in oxygen at 320°C resulted in particularly impressive ex-situ mass-specific oxygen evolution performance compared to the other deposition conditions. For these reasons, this chapter is dedicated to developing a greater understanding of this material. The reproducibility of synthesis in these conditions is explored, and a more thorough discussion around the electrochemical performance of this catalyst is discussed, drawing on comparisons from literature works on other IrO$_x$/ATO OER catalysts.*

The OER electrocatalytic activity of OMCD IrO$_x$/ATO that was synthesised at 320°C in oxygen exhibited outstanding OER performance. The synthesis of this particular catalyst was repeated, in order to check whether or not its OER performance was reproducible. EDX analysis revealed an Ir mass loading of 9.4 ± 0.5 and 8.9 ± 0.3 wt.% across two OMCD-batches of as-synthesised IrO$_x$/ATO catalyst, respectively. The reproducibility of the synthesis is clearly visible in ***Figure 7-1 (a)***: the Ir mass-specific oxygen evolution activity at 1.525 V vs. RHE was found to be 70 ± 7.0 A $g_{Ir}^{-1}$ for the first batch, whereas the second batch achieved 73 ± 10 A $g_{Ir}^{-1}$ at the same potential. These performances are a magnitude that was well over 5 times higher than the activity of the Elyst Ir75 IrO$_2$-TiO$_2$ commercial benchmark (10.4 ± 1.9 A $g_{Ir}^{-1}$).

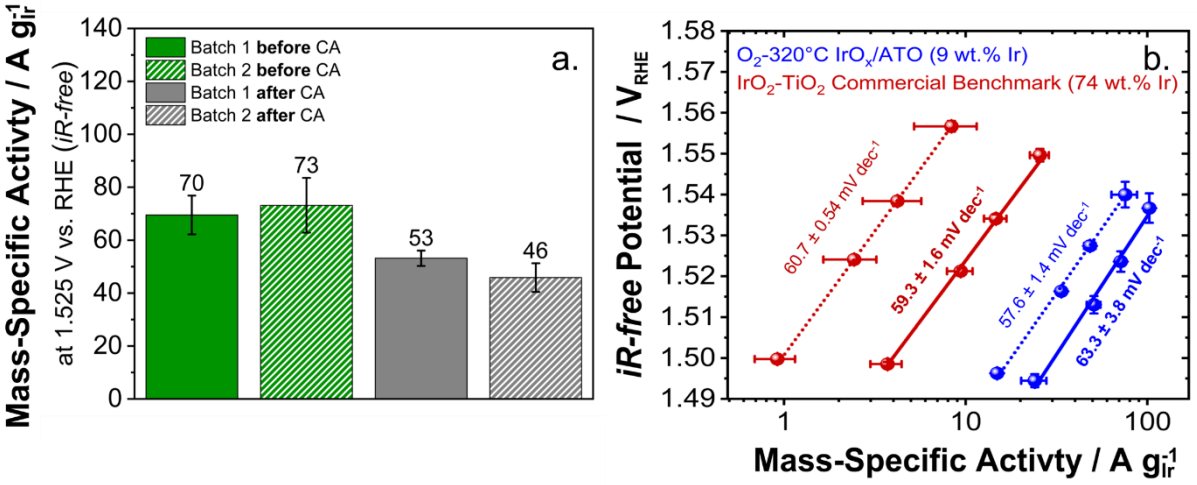


***Figure 7-1:*** *Mass-specific activity of two synthesis batches of OMCD IrO$_x$/ATO, before (green) and after (grey) stability evaluation by chronoamperometry (CA) (a). Mass-specific Tafel plots of OMCD IrO$_x$/ATO (average across two catalyst batches) and commercial Elyst Ir75 benchmark before (solid lines) and after stability evaluation (dotted lines) (b).*

After stability testing for 2 hours at 1.600 V vs. RHE, similar reproducibility was observed; here, batches 1 and 2 achieved mass-specific activities of 53 ± 2.9 and 46 ± 5.4 A $g_{Ir}^{-1}$, at 1.525 V vs. RHE, respectively. On average across the two catalyst batches, an overall relative loss of mass activity of ~31% was observed by $IrO_x$/ATO, and the $IrO_2$-$TiO_2$ commercial benchmark suffered a much larger loss of 76%. This is a promising outcome of the deposition method, as the more active $IrO_x$ nanoparticles of the OMCD $IrO_x$/ATO catalyst would be expected to be less stable than the more bulk-like $IrO_2$-$TiO_2$ benchmark. It is possible that the stability of OMCD $IrO_x$/ATO is as a consequence of a fortified interaction between the ATO support and $IrO_x$ nanoparticles, as a result of the thermal nature of the deposition process and as a result of the fact that the ATO was present during the synthesis of the $IrO_x$ particles. As mentioned earlier in the literature review, one of the drawbacks of wet synthesis methods is that in most cases, the iridium or iridium oxide nanoparticles are synthesised separately and then added to the ATO support at later stages in the synthesis process: this often results in a much weaker catalyst-support interaction than that which is observed in cases where the ATO support has been present during the synthesis of the $IrO_x$ nanoparticles (Spöri et al., 2017).

The Ir mass-specific oxygen evolution activity of $IrO_x$/ATO was investigated using chronoamperometric potential steps, where ***Figure 7-1(b)*** illustrates Tafel plots of the Ir mass-specific OER currents that were attained. Initially, our OMCD $IrO_x$/ATO exhibited a Tafel slope of 63 mV $dec^{-1}$ and this value changed to 58 mV $dec^{-1}$ after stability evaluation. Both values are comparable to Tafel slopes previously reported for unsupported $IrO_x$, e.g. 60 mV $dec^{-1}$ (Reier, Oezaslan & Strasser, 2012; Smith et al., 2014) as well as for $IrO_x$/ATO (52 to 60 mV $dec^{-1}$) (Liu et al., 2015; Oh et al., 2016; Ohno et al., 2019). A decrease in the value of the Tafel slope has previously been attributed to an increase in the degree of hydration of the $IrO_x$ catalytic surface (Minguzzi et al., 2015). As surface hydroxylation is strongly associated with the presence of $Ir^{3+}$ species (Geiger et al., 2016), this suggests that during stability evaluation (a 2-hour potential hold at 1.600 V vs. RHE) there is a potential-driven physicochemical change which takes place in the $IrO_x$ nanoparticles, possibly correlated with catalysing the OER, and resulting in an increased proportion of $Ir^{3+}$ species. From extrapolation of the initial Tafel fit of the OMCD $IrO_x$/ATO, an Ir mass-specific activity of 10 A $g_{Ir}^{-1}$ was obtained at a potential of 1.470 V vs. RHE (overpotential of 240 mV). For the Elyst Ir75 $IrO_2$-$TiO_2$ benchmark, the same activity value required a significantly higher potential of 1.524 V vs. RHE (overpotential of 294 mV). After stability evaluation, a similar trend was observed, where OMCD $IrO_x$/ATO required an overpotential of 256 mV to achieve a mass-specific activity of 10 A $g_{Ir}^{-1}$, whereas the commercial benchmark required an overpotential of 331 mV to achieve the same. Thus, the OER performance of the OMCD $IrO_x$/ATO catalyst was superior to the $IrO_2$-$TiO_2$ benchmark.

In the case of unsupported iridium oxides, it has been reported that amorphous iridium oxyhydroxides are a factor of 16-times more active than crystalline, rutile $IrO_2$ (Pfeifer, Jones, Vélez, et al., 2016). On this basis, it is interesting to note that our OMCD catalyst was highly active

towards OER, although both HR-STEM and XPS analyses illustrated that the dominating Ir phase in $IrO_x$/ATO was crystalline, rutile $IrO_2$. Unsupported, rutile $IrO_2$ is known to exhibit a much lower active surface area than amorphous $IrO_x$ (Pfeifer, Jones, Vélez, et al., 2016). Generally, small nanoparticles tend to have a higher quantity of exposed surface sites (edges, kinks, corners and steps), and a larger surface area to volume ratio per unit mass of metal; this results in higher catalytic activity than observed on bulk materials (Munnik, De Jongh & De Jong, 2015). In addition, dispersing such nanoparticles over suitable support materials can amplify these effects (van Santen, 2009). Therefore, a possible explanation for the outstanding OER activity combined with a high degree of crystallinity of the OMCD $IrO_x$/ATO is in an enhancement of the electrochemically active surface area both due to the geometry of rutile iridium (IV) oxide nanoparticles, and as a result of their uniform dispersion over the ATO support.

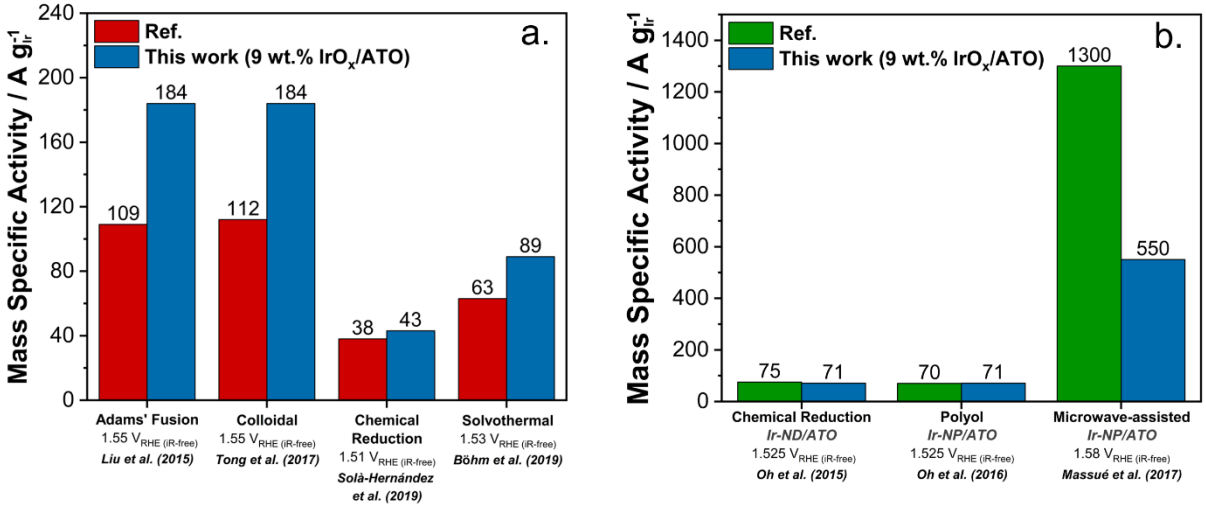


***Figure 7-2:*** *Literature comparisons for various works where iridium oxide (a) or metallic iridium (b) has been deposited on ATO support.*

For comparison of OMCD $IrO_x$/ATO with the activities of ATO-supported $IrO_x$ catalysts reported from other studies, a linear fit of the Tafel plot of ohmic-corrected Ir mass-specific OER currents was used to interpolate/extrapolate the activity values in this work to the corresponding potentials where these measurements were taken - see ***Figure 7-2*** above. It should be noted that only literature data where the *ex-situ* RDE method was utilised for OER catalyst characterisation were used in this comparison. ***Figure 7-2*** illustrates that the Ir mass-specific activity of OMCD $IrO_x$/ATO is on par with, or even exceeds, the literature reported activities of ATO-supported Ir-based electrocatalysts, with the exception of Massué et al. (2017). To discern the differences between the mass-activity achieved by OMCD $IrO_x$/ATO versus other works, it is necessary to understand that the performance of supported iridium-based OER catalysts is a function of various physical properties, such as the spatial distribution of $IrO_x$ over the support, the crystallinity and particle size of the deposited $IrO_x$ phases, as well as the oxidation state of the iridium. For instance, Liu et al. (2015) and Tong et al. (2017) prepared $IrO_x$ particles with sizes which ranged from 5-8 nm and 3-6 nm, where as in our work, smaller particle sizes of 1-5 nm were

achieved. Therefore, the approximately 1.7-times higher mass-activity observed at 1.550 V vs. RHE can possibly be attributed to OMCD $IrO_x$/ATO having a higher surface area, as a result of smaller particles. On the contrary, OMCD $IrO_x$/ATO demonstrated similar mass-specific activity to catalysts where $IrO_x$ nanoparticles were deposited onto ATO aerogel via chemical reduction (Solà-Hernández et al., 2019) and onto macroporous ATO using a hydrothermal method (Böhm et al., 2019). This is as a result of comparable $IrO_x$ particle sizes and related Ir oxidation states.

It is, however, difficult to make comparisons between reports where supported $IrO_x$ has been used, versus those where metallic Ir was deposited onto ATO support (Oh et al., 2015, 2016; Massué et al., 2017). It is known that metallic iridium becomes electrochemically activated and converted to amorphous iridium oxohydroxide during the application of an oxidising potential (Kötz, 1984; Saveleva et al., 2018). These species have been shown to exhibit much higher OER activity than thermally prepared iridium oxides, due to higher surface area and nature of the Ir species (Pfeifer, Jones, Vélez, et al., 2016). It is therefore encouraging that the mass-activity of OMCD $IrO_x$/ATO was comparable to these studies. However, an approximately 2.5 times larger Ir mass-specific activity at a potential of 1.580 V vs. RHE was achieved by Massué et al. (2017), where an ATO support with optimised surface area and electronic conductivity was synthesised. This would suggest that the performance of OMCD $IrO_x$/ATO could potentially be further improved by optimisation of the ATO support on the basis of its electronic conductivity and surface area.

# Chapter 8: Towards Further Understanding of the OMCD Process

*As seen in Chapter 7, organometallic chemical deposition is a viable method to produce high-performance iridium oxide supported on ATO. While this is the case, it was observed that the achieved iridium loading was approximately half of the nominal loading. This inspired the development of two optimisation strategies improve the efficiency of the deposition process.*

## 8.1 STRATEGIES FOR SYNTHESIS OPTIMISATION

As discussed in **Chapter 6**, a significant loss of iridium takes place during the organometallic deposition process. From TGA studies, it was seen that the $Ir(acac)_3$ precursor vaporises from 200-250°C. The OMCD reactor is a fairly long (56 cm) tube where only the ends are sealed during the deposition process. The ATO+$Ir(acac)_3$ powder mixture is placed in the centre of this tube, and therefore a likely explanation for the iridium losses observed during the syntheses is that: between vaporisation of the precursor and iridium deposition on the ATO support, the precursor in the vapour phase has had an opportunity to move through the entire reactor length, as the reactor heats up to the desired temperature, depositing iridium along the reactor walls and not on the ATO support as intended. This would explain the results which were obtained in deposition in both oxygen and argon environments, where at higher temperatures, lower iridium loadings were achieved.

In an attempt to minimise these iridium losses, two further synthesis strategies were explored. The first involved the filling the reactor to 80% volume capacity with the ATO+$Ir(acac)_3$ mixture, in order to increase the likelihood of the $Ir(acac)_3$ precursor vapour decomposing on the ATO support, as opposed to on the reactor walls. It should be noted that for this particular strategy, a low nominal iridium loading of 5 wt.% was targeted, owing to the large amount of precursor that would have been required for a 20 wt.% nominal iridium loading to achieve 80% full capacity of the reactor. The second strategy was aimed at reducing the time that the iridium precursor spends in the vapour phase, prior to reaching the temperature where decomposition occurs. To do this, the sealed reactor tube was removed from the furnace after the removal of water at 100°C, and prior to the temperature ramp to the desired deposition temperature. The reactor tube was then re-inserted into the furnace once the desired deposition temperature had been reached, causing a much more rapid heat up of the ATO+$Ir(acac)_3$ reaction mixture. Both these strategies were

explored in an oxygen environment at 320°C for comparison to the catalyst which had the best OER performance and was fully characterised in **Chapter 6** and **Chapter 7**.

## 8.2 RESULTS

### 8.2.1 Iridium Mass Loading by Energy Dispersive X-ray Spectroscopy (EDX)

The iridium mass loading achieved by the synthesis optimisation described above was investigated using EDX spectroscopy, and the results are illustrated in ***Table 8-1*** below, where results for the original synthesis in oxygen at 320°C across two synthesis batches are also shown for comparative purposes.

***Table 8-1****: Ir mass loadings achieved by synthesis optimisation in oxygen at 320°C.*

| | **Nominal Ir loading / wt.%** | **Ir loading / wt.%** | **Error / wt.%** | **Iridium Yield / %** |
|---|---|---|---|---|
| $O_2$-320°C, Batch 1 | 20 | 9.4 | ± 0.5 | 47 |
| $O_2$-320°C, Batch 2 | 20 | 8.9 | ± 0.3 | 44 |
| $O_2$-320°C, No Ramp Time | 20 | 10.1 | ± 0.2 | 51 |
| $O_2$-320°C, 80% Full Reactor | 5 | 3.3 | ± 0.02 | 66 |

The results above indicate that a small improvement in iridium yield was obtained by minimising the heating time of the reactor, by inserting it directly into the furnace at 320°C; this synthesis achieved an iridium loading of 10.1 wt.%, as opposed to 9.4 and 8.9 wt.% Ir achieved in the original synthesis method. A much larger improvement of iridium yield was observed in the 80% full reactor strategy; here it was seen that a 66% iridium yield was attained, a significant improvement compared to the original yield of ~46%.

### 8.2.2 Electrochemical Performance

The OER electrochemical performance of the two synthesis optimisation strategies was evaluated, with results in ***Figure 8-1*** below.

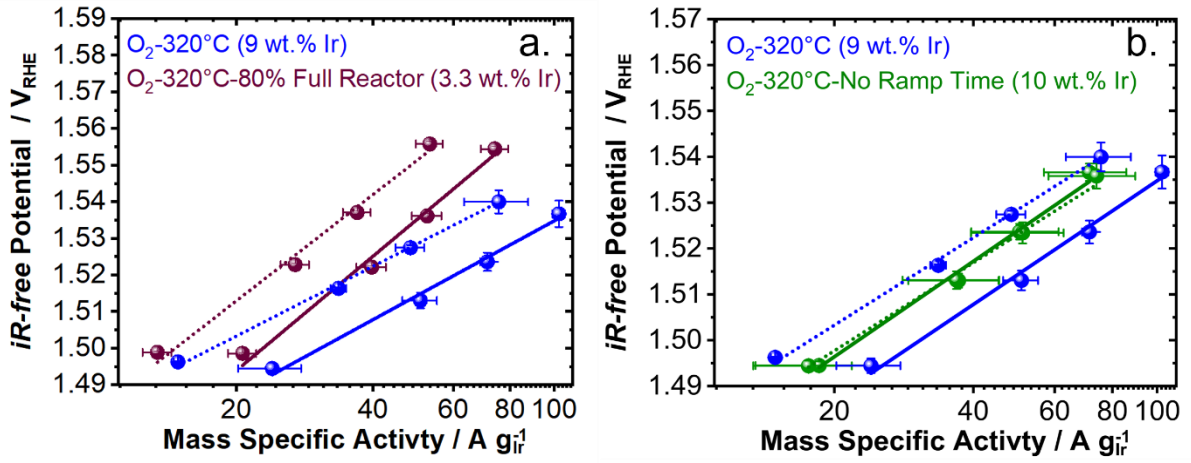


***Figure 8-1:*** *Mass-specific Tafel plots of optimised OMCD $IrO_x$/ATO before (solid lines) and after stability evaluation (dotted lines) (a). Mass-specific activity of two synthesis batches of optimised syntheses of OMCD $IrO_x$/ATO, before and after stability evaluation by chronoamperometry (CA) (b).*

The results shown in ***Figure 8-2*** are highly interesting. The large batch of catalyst synthesised in the 80% full reactor performs reasonably well, with a mass-specific OER activity of 40 A $g_{Ir}^{-1}$ at 1.525 V vs. RHE. The mass-activity of this catalyst is lower than that achieved by the original catalyst at the same potential (71 A $g_{Ir}^{-1}$), in the same synthesis conditions, however; this is likely to be as a result of the lower iridium loading in this catalyst (3.3 wt.% Ir) versus the original preparation in oxygen at 320°C (9 wt.% Ir). A relative loss of mass activity of ~33% at 1.525 V vs. RHE was observed after 2 hours at a potential of 1.600 V vs. RHE in the catalyst prepared in the 80% full reactor, as opposed to the ~31% loss observed in the original catalyst. This is a very similar result and would strongly imply that the oxidation states and particle size of the deposited Ir species in this catalyst versus in the original $O_2$-320°C are very similar. This in itself shows the reproducibility of OMCD in oxygen at 320°C. As preparation in the 80% full reactor produced a catalyst with a lower iridium loading than in the original synthesis, there is a larger ATO:$IrO_x$ ratio, and this is expected to provide a small enhancement in stability, because ATO generally exhibits a much lower electrical conductivity than that observed in iridium oxides (Puthiyapura et al., 2014). The Tafel slope of the catalyst prepared in the 80% full reactor is also significantly steeper than that observed in the original catalyst; this would suggest that the catalysis of the OER on this catalyst is less efficient than in the original material. This once again can be explained based on the differences in overall electrical conductivity that are likely to exist across the two materials. Naturally, the more conductive catalyst (the original catalyst with 9 wt% Ir) would exhibit a higher catalytic efficiency than the catalyst with less iridium (3.3 wt.% Ir).

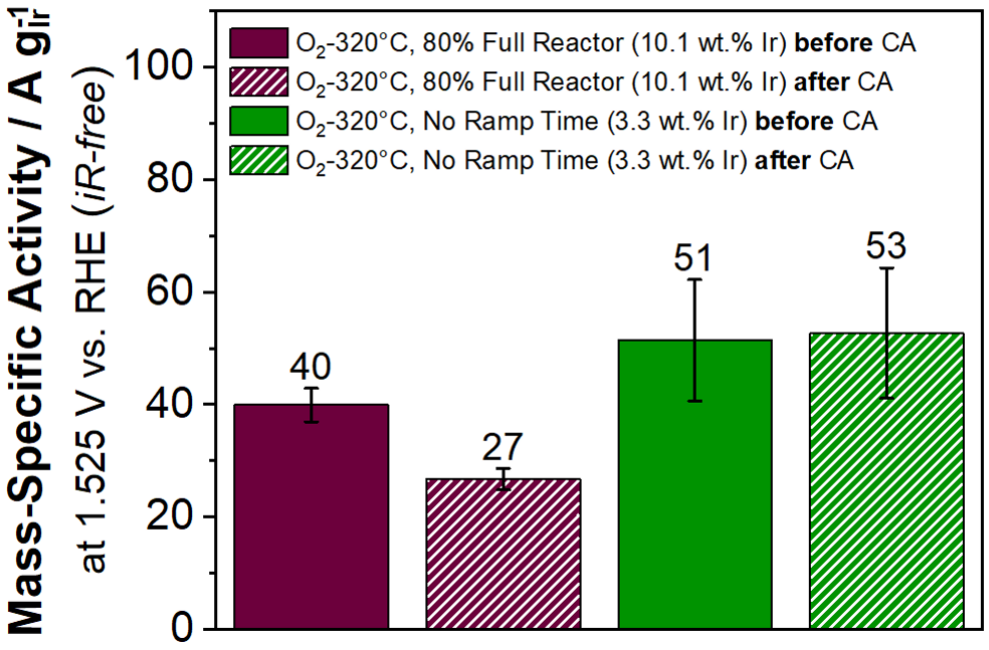


***Figure 8-2:*** *Mass-specific activity of two synthesis batches of optimised syntheses of OMCD $IrO_x$/ATO, before and after stability evaluation by chronoamperometry (CA).*

The most striking observation of the catalyst which was synthesised with the exclusion of the ramp to the deposition temperature, is that virtually no loss of mass-specific activity was observed after subjection to the stability test at 1.600 V vs. RHE for a period of 2 hours, as seen by the almost identical Tafel slopes and mass-activity at 1.525 V vs. RHE for this catalyst in ***Figure 8-2***. The mass-specific activity attained prior to stability testing was 50 A $g_{Ir}^{-1}$, a lower value than that observed in the original catalyst preparation conditions (71 A $g_{Ir}^{-1}$). While in-depth physical characterisation was not performed on the optimised catalysts, as a result of time constraints, it is possible that in eliminating the ramp to the deposition temperature, the $Ir(acac)_3$ precursor is decomposed very rapidly into metallic iridium.

# Chapter 9: Conclusions and Recommendations

*This chapter summarises the main conclusions from this work and offers some suggestions and recommendations for further work.*

This thesis has demonstrated a simple and reproducible method for the deposition of crystalline iridium oxide nanoparticles on ATO, in a one-step, organometallic chemical deposition (OMCD) process. Various deposition temperatures were explored in oxygen and argon atmospheres and here it was seen that the $IrO_x$/ATO electrocatalyst which was synthesised in oxygen at 320°C, containing 9 wt.% iridium, exhibited outstanding OER performance, which was superior to commercially available $IrO_2$-$TiO_2$ and comparable with ATO-supported iridium-based catalysts reported from other studies. The synthesis in 320°C in oxygen was also seen to be reproducible. Thus, OMCD has proven to be a facile and robust method to deposit highly dispersed $IrO_2$ nanoparticles onto oxide support, with competitive OER performance.

While synthesis at 320°C in argon was also seen to be effective, larger particles were deposited, in comparison to preparation in the same temperature in oxygen. In addition, it was seen that preparation at 620°C in oxygen resulted in the formation of iridium sub-oxides, and that preparation in argon at 620°C resulted in the segregation of antimony from the ATO support, and the formation of metallic iridium species. Across all the prepared catalysts, it was observed that the nominal iridium loading of 20 wt.% was never reached, and as a result, some optimisations to the synthesis method were carried out.

As a route to further improve the OMCD process, two strategies were explored in the best catalyst preparation conditions, deposition in oxygen at 320°C. These were the elimination of the reactor heating time, and the maximisation of the contact between the ATO support and decomposed iridium acetylacetonate precursor by filling of the reactor chamber with the support-precursor mixture to 80% capacity. Elimination of the reactor heating had a minor effect on the iridium loading achieved, this catalyst exhibited lower mass-specific activity than the original catalyst which was prepared at 320°C in oxygen with a heating rate of 5°C $min^{-1}$. Reasons for this are likely to be as a result of incomplete $Ir(acac)_3$ decomposition. On the other hand, this catalyst exhibited a particularly interesting result from the perspective of OER stability, where barely any loss of mass-specific activity after subjection to 1.6 V vs. RHE, in comparison to the original catalyst, which suffered a relative loss of 31% after the same test. The catalyst prepared at 80%-full reactor capacity demonstrated a 20% improvement in the iridium deposition yield. Further detailed characterisation into the optimised catalysts mentioned above is necessary, in order to elucidate the particle size and oxidation states of the deposited $IrO_x$ particles.

Another means to lower the Ir losses suffered during OMCD could be to perform the synthesis under elevated oxygen partial pressures. Higher $O_2$ pressures could enhance the rate of $Ir(acac)_3$ decomposition over the rate of its evaporation, increasing the amount of iridium which is deposited on the ATO support, avoiding the evaporation of the precursor away from the support. However, in the case of deposition in argon, OMCD at higher pressures is unlikely to have any beneficial consequences on the Ir yield achieved by the deposition. Argon provides an inert reaction atmosphere and therefore its presence has no effect on the decomposition rate of the $Ir(acac)_3$ precursor. In addition, as neither argon nor oxygen can influence the rate of evaporation of the precursor, increasing the partial pressure of argon in the OMCD process would have no effect on the Ir yield achieved during deposition.

While this thesis has provided some excellent insight into the application of a novel synthesis approach for the deposition of $IrO_x$ onto ATO support, there are several aspects of this work that can be explored further, to develop an even better understanding towards this synthesis technique. $Ir(acac)_3$ is a promising precursor, however, to date, it is still one of the most expensive iridium precursors on the market. Therefore, exploration of alternative, cheaper precursors such as iridium III and IV chloride need to be examined. The OMCD method has proven that it is viable for the deposition of iridium oxide on ATO, however, its use with other support materials also needs to be explored.

This study did not utilise synchrotron characterisation methods, and such methods could be extremely useful in elucidating more information pertaining to the geometry and structure of the OMCD $IrO_x$/ATO catalysts. Extended X-ray fine structure (EXAFS) and X-ray absorption near-edge spectroscopy (XANES) could be helpful to develop a greater understanding towards the geometry and local structure of the synthesised catalytic materials. Furthermore, anomalous small angle X-ray scattering (ASAXS) could assist with obtaining a more accurate indication of the $IrO_x$ nanoparticle size; as the particles are too small to be measured by XRD, small angle X-ray scattering could greatly aid with this. The results in this thesis are very interesting however it would be even more meaningful to acquire an insight towards the processes which occur on the OMCD $IrO_x$/ATO catalyst during OER conditions. While several works have investigated the processes which occur on Ir metal on ATO during OER, it would be interesting to observe the changes which occur when an iridium oxide phase which contains predominantly Ir IV is present on ATO support. Such a study could provide further insight on the catalyst-support interactions which have been shown to be present in $IrO_x$/ATO catalytic materials during oxygen evolution.

# References


Abbott, D.F., Lebedev, D., Waltar, K., Povia, M., Nachtegaal, M., Fabbri, E., Copéret, C. & Schmidt, T.J. 2016. Iridium oxide for the oxygen evolution reaction: Correlation between particle size, morphology, and the surface hydroxo layer from operando XAS. *Chemistry of Materials*. 28(18):6591–6604.

Asadian, M. 2012. The Influence of Atmosphere on Oxides Crystal Growth. *Modern Aspects of Bulk Crystal and Thin Film Preparation*.

Audichon, T., Mayousse, E., Morisset, S., Morais, C., Comminges, C., Napporn, T.W. & Kokoh, K.B. 2014. Electroactivity of RuO2-IrO2 mixed nanocatalysts toward the oxygen evolution reaction in a water electrolyzer supplied by a solar profile. *International Journal of Hydrogen Energy*. 39(30):16785–16796.

Binninger, T., Mohamed, R., Waltar, K., Fabbri, E., Levecque, P., Kötz, R. & Schmidt, T.J. 2015. Thermodynamic explanation of the universal correlation between oxygen evolution activity and corrosion of oxide catalysts. *Scientific Reports*. 5(February):1–7.

Böhm, D., Beetz, M., Schuster, M., Peters, K., Hufnagel, A.G., Döblinger, M., Böller, B., Bein, T., et al. 2019. Efficient OER Catalyst with Low Ir Volume Density Obtained by Homogeneous Deposition of Iridium Oxide Nanoparticles on Macroporous Antimony- Doped Tin Oxide Support. *Advanced Functional Materials*. (October, 25):1906670.

Buttler, A. & Spliethoff, H. 2018. Current status of water electrolysis for energy storage, grid balancing and sector coupling via power-to-gas and power-to-liquids: A review. *Renewable and Sustainable Energy Reviews*. 82(February 2017):2440–2454.

Che, M. & Védrine, J.C. 2012. *Characterization of Solid Materials and Heterogeneous Catalysts: From Structure to Surface Reactivity, Volume 1&2*.

Cherevko, S., Geiger, S., Kasian, O., Kulyk, N., Grote, J.P., Savan, A., Ratna, B., Merzlikin, S., et al. 2016. Oxygen and hydrogen evolution reactions on Ru, RuO2, Ir, and IrO2 thin film electrodes in acidic and alkaline electrolytes: A comparative study on activity and stability. *Catalysis Today*. 262:170–180.

Elangovan, E. & Ramamurthi, K. 2005. A study on low cost-high conducting fluorine and antimony-doped tin oxide thin films. *Applied Surface Science*. 249(1–4):183–196.

Fabbri, E., Habereder, A., Waltar, K., Kötz, R. & Schmidt, T.J. 2014. Developments and perspectives of oxide-based catalysts for the oxygen evolution reaction. *Catalysis Science and Technology*. 4(11):3800–3821.

Fuentes, R.E., Farell, J. & Weidner, J.W. 2011. Multimetallic electrocatalysts of Pt, Ru, and Ir supported on anatase and rutile TiO2 for oxygen evolution in an acid environment. *Electrochemical and Solid-State Letters*. 14(3):62–64.

Garcia, A.C. & Koper, M.T.M.M. 2018. Effect of Saturating the Electrolyte with Oxygen on the Activity for the Oxygen Evolution Reaction. *ACS Catalysis*. 8(10):9359–9363.

Garcia, J.R.V. & Goto, T. 2003. Chemical Vapor Deposition of Iridium, Platinum, Rhodium and Palladium. *Materials Transactions*. 44(9):1717–1728.

Geiger, S., Kasian, O., Shrestha, B.R., Mingers, A.M., Mayrhofer, K.J.J. & Cherevko, S. 2016.

Activity and stability of electrochemically and thermally treated iridium for the oxygen evolution reaction. *Journal of the Electrochemical Society*. 163(11):F3132–F3138.

Grimaud, A., Diaz-morales, O., Han, B., Hong, W.T., Lee, Y., Giordano, L., Stoerzinger, K.A., Koper, M.T.M., et al. 2017. oxides to catalyse oxygen evolution. *Nature Chemistry*. 9(5):457–465.

Grimaud, A., Diaz-Morales, O., Han, B., Hong, W.T., Lee, Y.L., Giordano, L., Stoerzinger, K.A., Koper, M.T.M., et al. 2017. Activating lattice oxygen redox reactions in metal oxides to catalyse oxygen evolution. *Nature Chemistry*. 9(5):457–465.

Hamalainen, J., Kemell, M., Munnik, F., Kreissig, U., Ritala, M. & Leskela, M. 2008. Atomic layer deposition of iridium oxide thin films from Ir(acac)(3) and ozone. *Chemistry of Materials*. 20(9):2903–2907.

Hämäläinen, J., Ritala, M. & Leskelä, M. 2014. Atomic layer deposition of noble metals and their oxides. *Chemistry of Materials*. 26(1):786–801.

Hu, W., Chen, S. & Xia, Q. 2014. IrO2/Nb-TiO2 electrocatalyst for oxygen evolution reaction in acidic medium. *International Journal of Hydrogen Energy*. 39(13):6967–6976.

Jackson, C., Conrad, O. & Levecque, P. 2017. Systematic Study of Pt-Ru/C Catalysts Prepared by Chemical Deposition for Direct Methanol Fuel Cells. *Electrocatalysis*. 8(3):224–234.

Kemell, M., Pore, V., Ritala, M. & Leskelä, M. 2006. Ir/Oxide/Cellulose Composites for Catalytic Purposes Prepared by Atomic Layer Deposition. *Chemical Vapor Deposition*. 12(7):419–422.

Kim, Y.T., Lopes, P.P., Park, S.A., Lee, A.Y., Lim, J., Lee, H., Back, S., Jung, Y., et al. 2017. Balancing activity, stability and conductivity of nanoporous core-shell iridium/iridium oxide oxygen evolution catalysts. *Nature Communications*. 8(1):1–8.

Kothari, R., Buddhi, D. & Sawhney, R.L. 2008.

Kötz, R. 1984. Anodic Iridium Oxide Films. *Journal of The Electrochemical Society*. 131(1):72.

Lebedev, D. & Copéret, C. 2019. Small, narrowly distributed iridium nanoparticles supported on indium tin oxide for efficient anodic water oxidation. *ACS Applied Energy Materials*. 2(1):196–200.

Liu, G., Xu, J., Wang, Y. & Wang, X. 2015. An oxygen evolution catalyst on an antimony doped tin oxide nanowire structured support for proton exchange membrane liquid water electrolysis. *Journal of Materials Chemistry A*. 3(41):20791–20800.

Locatelli, F., Didillon, B., Uzio, D., Niccolai, G., Candy, J.P. & Basset, J.M. 2000. Preparation and characterization of small silica-supported iridium particles from iridium trisacetylacetonate precursor. *Journal of Catalysis*. 193(1):154–160.

Maillard, F., Bonnefont, A. & Micoud, F. 2011. An EC-FTIR study on the catalytic role of Pt in carbon corrosion. *Electrochemistry Communications*. 13(10):1109–1111.

Marshall, A.T. & Haverkamp, R.G. 2010. Electrocatalytic activity of IrO2-RuO2 supported on Sb-doped SnO2 nanoparticles. *Electrochimica Acta*. 55(6):1978–1984.

Massué, C., Pfeifer, V., Huang, X., Noack, J., Tarasov, A., Cap, S. & Schlögl, R. 2017. High-Performance Supported Iridium Oxohydroxide Water Oxidation Electrocatalysts. *ChemSusChem*. 10(9):1943–1957.

Minguzzi, A., Locatelli, C., Lugaresi, O., Achilli, E., Cappelletti, G., Scavini, M., Coduri, M., Masala, P., et al. 2015. Easy Accommodation of Different Oxidation States in Iridium Oxide Nanoparticles with Different Hydration Degree as Water Oxidation Electrocatalysts. *ACS Catalysis*. 5(9):5104–

5115.

Mohamed, R., Binninger, T., Kooyman, P.J., Hoell, A., Fabbri, E., Patru, A., Heinritz, A., Schmidt, T.J., et al. 2018. Facile deposition of Pt nanoparticles on Sb-doped SnO2 support with outstanding active surface area for the oxygen reduction reaction. *Catalysis Science & Technology*. 8:2672–2685.

Munnik, P., De Jongh, P.E. & De Jong, K.P. 2015. Recent Developments in the Synthesis of Supported Catalysts. *Chemical Reviews*. 115(14):6687–6718.

Nassreddine, S., Bergeret, G., Jouguet, B., Geantet, C. & Piccolo, L. 2010. Operando study of iridium acetylacetonate decomposition on amorphous silica-alumina for bifunctional catalyst preparation. *Physical Chemistry Chemical Physics*. 12(28):7812–7820.

Niemantsverdriet, J.W. 2007. *Spectroscopy in Catalysis: An Introduction: Third Edition*.

Nong, H.N., Gan, L., Willinger, E., Teschner, D. & Strasser, P. 2014. IrOx core-shell nanocatalysts for cost- and energy-efficient electrochemical water splitting. *Chemical Science*. 5(8):2955–2963.

Nütz, T., Zum Felde, U. & Haase, M. 1999. Wet-chemical synthesis of doped nanoparticles: Blue-colored colloids of n-doped SnO2:Sb. *Journal of Chemical Physics*. 110(24):12142–12150.

Oakton, E., Lebedev, D., Povia, M., Abbott, D.F., Fabbri, E., Fedorov, A., Nachtegaal, M., Cope, C., et al. 2017. IrO2-TiO2: A High-Surface-Area, Active, and Stable Electrocatalyst for the Oxygen Evolution Reaction. *ACS Catalysis*. 7(4):2346–2352.

Oh, H.S., Nong, H.N., Reier, T., Gliech, M. & Strasser, P. 2015. Oxide-supported Ir nanodendrites with high activity and durability for the oxygen evolution reaction in acid PEM water electrolyzers. *Chemical Science*. 6(6):3321–3328.

Oh, H.S., Nong, H.N., Reier, T., Bergmann, A., Gliech, M., Ferreira De Araújo, J., Willinger, E., Schlögl, R., et al. 2016. Electrochemical Catalyst-Support Effects and Their Stabilizing Role for IrOxNanoparticle Catalysts during the Oxygen Evolution Reaction. *Journal of the American Chemical Society*. 138(38):12552–12563.

Ohno, H., Nohara, S., Kakinuma, K., Uchida, M. & Uchida, H. 2019. Effect of electronic conductivities of iridium oxide/doped SnO 2 oxygen-evolving catalysts on the polarization properties in proton exchange membrane water electrolysis. *Catalysts*. 9(1):5–7.

Owe, L.E., Tsypkin, M., Wallwork, K.S., Haverkamp, R.G. & Sunde, S. 2012. Iridium-ruthenium single phase mixed oxides for oxygen evolution: Composition dependence of electrocatalytic activity. *Electrochimica Acta*. 70:158–164.

Pfeifer, V., Jones, T.E., Wrabetz, S., Massué, C., Velasco Vélez, J.J., Arrigo, R., Scherzer, M., Piccinin, S., et al. 2016. Reactive oxygen species in iridium-based OER catalysts. *Chemical Science*. 7(11):6791–6795.

Pfeifer, V., Jones, T.E., Velasco Vélez, J.J., Massué, C., Greiner, M.T., Arrigo, R., Teschner, D., Girgsdies, F., et al. 2016. The electronic structure of iridium oxide electrodes active in water splitting. *Physical Chemistry Chemical Physics*. 18(4):2292–2296.

Pfeifer, V., Jones, T.E., Vélez, J.J.V., Massué, C., Arrigo, R., Teschner, D., Girgsdies, F., Scherzer, M., et al. 2016. The electronic structure of iridium and its oxides. *Surface and Interface Analysis*. 48(5):261–273.

Puthiyapura, V.K., Mamlouk, M., Pasupathi, S., Pollet, B.G. & Scott, K. 2014. Physical and electrochemical evaluation of ATO supported IrO2catalyst for proton exchange membrane water electrolyser. *Journal of Power Sources*. 269:451–460.

Reier, T., Oezaslan, M. & Strasser, P. 2012. Electrocatalytic oxygen evolution reaction (OER) on Ru, Ir, and pt catalysts: A comparative study of nanoparticles and bulk materials. *ACS Catalysis*. 2(8):1765–1772.

Rozain, C., Mayousse, E., Guillet, N. & Millet, P. 2016. Influence of iridium oxide loadings on the performance of PEM water electrolysis cells: Part I-Pure IrO 2 -based anodes. *Applied Catalysis B: Environmental*. 182:153–160.

Rozmus, M., Blicharski, M. & Dymek, S. 2006. Scanning and transmission electron microscopy microstructure characterization of mechanically alloyed Nb-Ti-Al alloys. *Journal of Microscopy*. 224(1):58–61.

van Santen, R.A. 2009. Insensitive Catalytic Relationships. *Accounts of Chemical Research*. 42(1):57–66.

Sapountzi, F.M., Gracia, J.M., Weststrate, C.J.K., Fredriksson, H.O.A. & Niemantsverdriet, J.W.H. 2017. Electrocatalysts for the generation of hydrogen , oxygen and synthesis gas. *Progress in Energy and Combustion Science*. 58:1–35.

Sasaki, K., Takasaki, F., Noda, Z., Hayashi, S., Shiratori, Y. & Ito, K. 2010. Alternative electrocatalyst support materials for polymer electrolyte fuel cells. *ECS Transactions*. 33(1):473–482.

Saveleva, V.A., Wang, L., Teschner, D., Jones, T., Gago, A.S., Friedrich, K.A., Zafeiratos, S., Schlögl, R., et al. 2018. Operando Evidence for a Universal Oxygen Evolution Mechanism on Thermal and Electrochemical Iridium Oxides. *Journal of Physical Chemistry Letters*. 9(11):3154–3160.

Saveleva, V.A., Wang, L., Kasian, O., Batuk, M., Hadermann, J., Gallet, J.-J., Bournel, F., Alonso-Vante, P.N., et al. 2020. Insight into the Mechanisms of High Activity and Stability of Iridium Supported on Antimony-Doped Tin Oxide Aerogel for Anodes of Proton Exchange Membrane Water Electrolysers. *ACS Catalysis*.

Schmidt, T.J. 2012. Electrocatalysis in Polymer Electrolyte Fuel Cells: From Fundamentals to Applications. *ECS Transactions*. 45(2):3–14.

Silvennoinen, R.J., Jylhä, O.J.T., Lindblad, M., Österholm, H. & Krause, A.O.I. 2007. Supported iridium catalysts prepared by atomic layer deposition: Effect of reduction and calcination on activity in toluene hydrogenation. *Catalysis Letters*. 114(3–4):135–144.

Silvennoinen, R.J., Jylhä, O.J.T., Lindblad, M., Sainio, J.P., Puurunen, R.L. & Krause, A.O.I. 2007. Atomic layer deposition of iridium(III) acetylacetonate on alumina, silica-alumina, and silica supports. *Applied Surface Science*. 253(9):4103–4111.

Smith, R.D.L., Sporinova, B., Fagan, R.D., Trudel, S. & Berlinguette, C.P. 2014. Facile photochemical preparation of amorphous iridium oxide films for water oxidation catalysis. *Chemistry of Materials*. 26(4):1654–1659.

Solà-Hernández, L., Claudel, F., Maillard, F. & Beauger, C. 2019. Doped tin oxide aerogels as oxygen evolution reaction catalyst supports. *International Journal of Hydrogen Energy*. 44(45):24331–24341.

Spöri, C., Kwan, J.T.H., Bonakdarpour, A., Wilkinson, D.P. & Strasser, P. 2017. The Stability Challenges of Oxygen Evolving Catalysts: Towards a Common Fundamental Understanding and Mitigation of Catalyst Degradation. *Angewandte Chemie - International Edition*. 56(22):5994–6021.

Spöri, C., Briois, P., Nong, H.N., Reier, T., Billard, A., Kühl, S., Teschner, D. & Strasser, P. 2019. Experimental Activity Descriptors for Iridium-Based Catalysts for the Electrochemical Oxygen Evolution Reaction (OER). *ACS Catalysis*. 9(8):6653–6663.

Sun, Y.M., Endle, J.P., Smith, K., Whaley, S., Mahaffy, R., Ekerdt, J.G., White, J.M. & Hance, R.L. 1999. Iridium film growth with iridium tris-acetylacetonate: Oxygen and substrate effects. *Thin Solid Films*. 346(1):100–107.

Taylor, S., Fabbri, E., Levecque, P., Schmidt, T.J. & Conrad, O. 2016. The Effect of Platinum Loading and Surface Morphology on Oxygen Reduction Activity. *Electrocatalysis*. 7(4):287–296.

Tong, J., Liu, Y., Peng, Q., Hu, W. & Wu, Q. 2017. An efficient Sb-SnO 2 -supported IrO 2 electrocatalyst for the oxygen evolution reaction in acidic medium. *Journal of Materials Science*. 52(23):13427–13443.

Vargas Garcia, J.R., Goto, T., Garcia, J.R.V. & Goto, T. 2003. Chemical Vapor Deposition of Iridium, Platinum, Rhodium and Palladium. *Materials Transactions*. 44(9):1717–1728.

de Vasconcelos, B.R. & Lavoie, J.M. 2019. Recent advances in power-to-X technology for the production of fuels and chemicals. *Frontiers in Chemistry*. 7(JUN):1–24.

Vasilyev, V.Y., Morozova, N.B., Basova, T. V., Igumenov, I.K. & Hassan, A. 2015. Chemical vapour deposition of Ir-based coatings: Chemistry, processes and applications. *RSC Advances*. 5(41):32034–32063.

Walsh, T.A., Bur, J.A., Kim, Y.-S., Lu, T.-M. & Lin, S.-Y. 2009. High-temperature metal coating for modification of photonic band edge position. *Journal of the Optical Society of America B*. 26(7):1450.

Wei, C., Rao, R.R., Peng, J., Huang, B., Stephens, I.E.L.L., Risch, M., Xu, Z.J. & Shao-Horn, Y. 2019. Recommended Practices and Benchmark Activity for Hydrogen and Oxygen Electrocatalysis in Water Splitting and Fuel Cells. *Advanced Materials*. 1806296:1–24.

Yu, H., Danilovic, N., Wang, Y., Willis, W., Poozhikunnath, A., Bonville, L., Capuano, C., Ayers, K., et al. 2018. Nano-size IrOx catalyst of high activity and stability in PEM water electrolyzer with ultra-low iridium loading. *Applied Catalysis B: Environmental*. 239(May):133–146.

Zhang, J. & Gao, L. 2004. Synthesis of antimony-doped tin oxide (ATO) nanoparticles by the nitrate-citrate combustion method. *Materials Research Bulletin*. 39(14–15):2249–2255.

# Appendix A: Experimental

## A.1 EDX CALIBRATION GRAPH

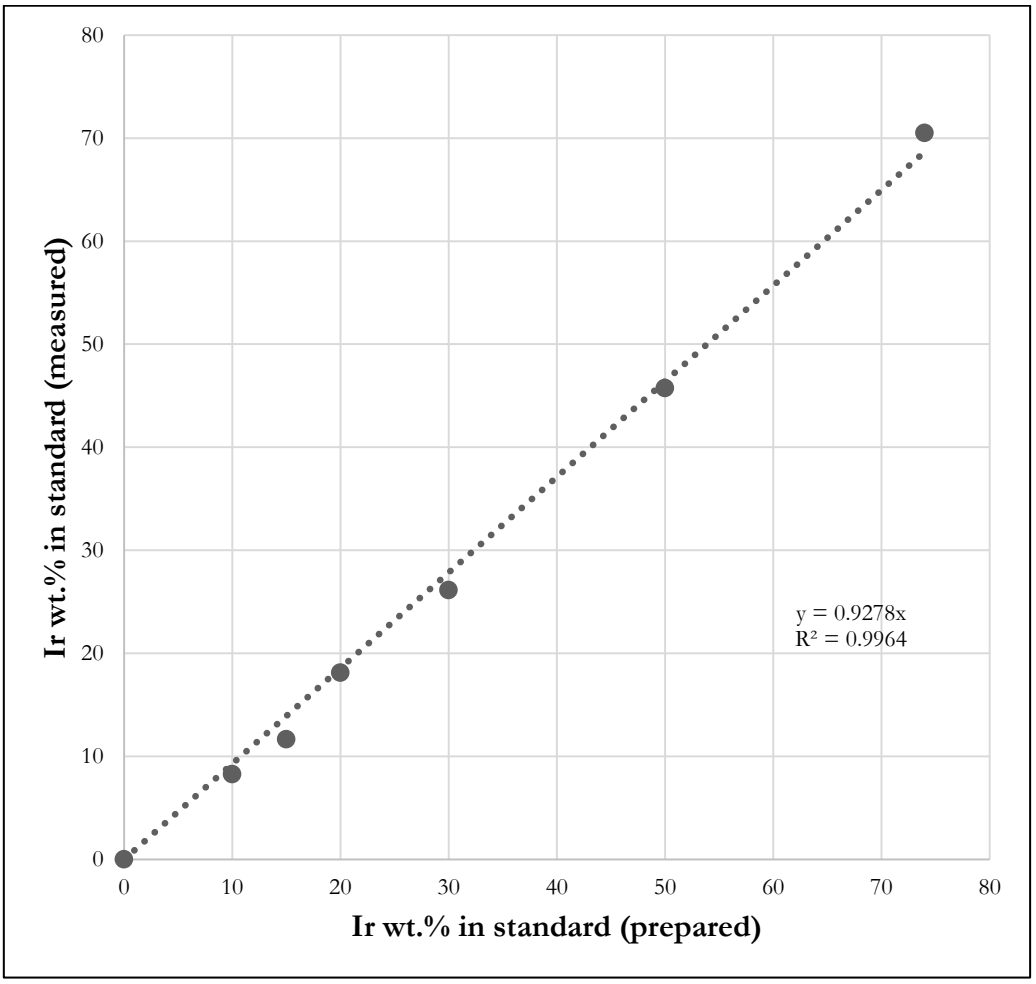


***Figure A-1:*** *EDX calibration graph showing measured Ir mass loading by EDX versus the known Ir mass loading in the prepared standards.*

# Appendix B: Physical Characterisation

## B.1 LATTICE SPACING ANALYSIS FOR CATALYST $O_2$-320°C

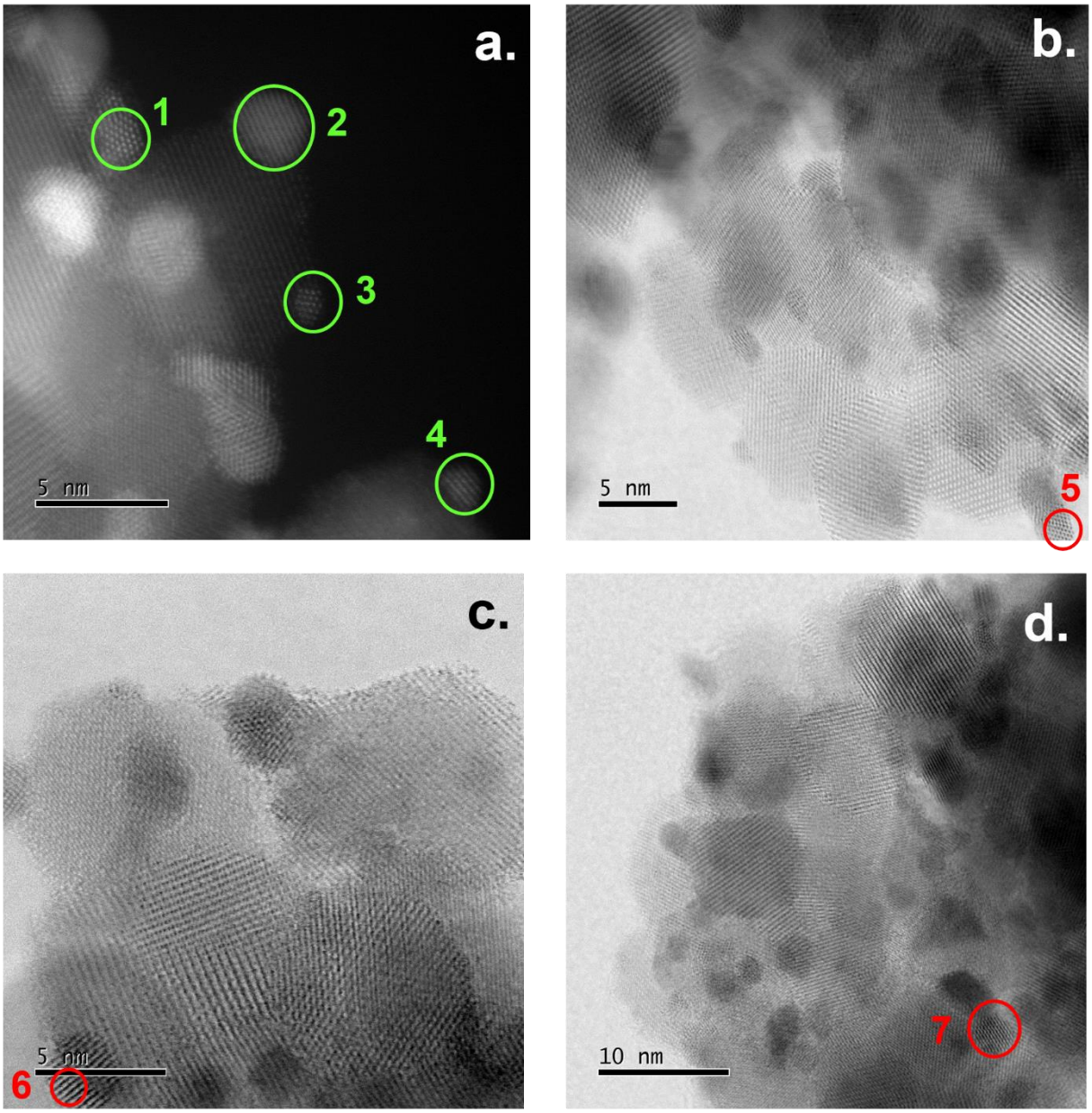


***Figure B-1:*** *HR-STEM images used for determination of lattice spacings in OMCD $O_2$-320°C $IrO_x$ particles.*

## B.2 LATTICE SPACING ANALYSIS FOR CATALYST Ar-320°C

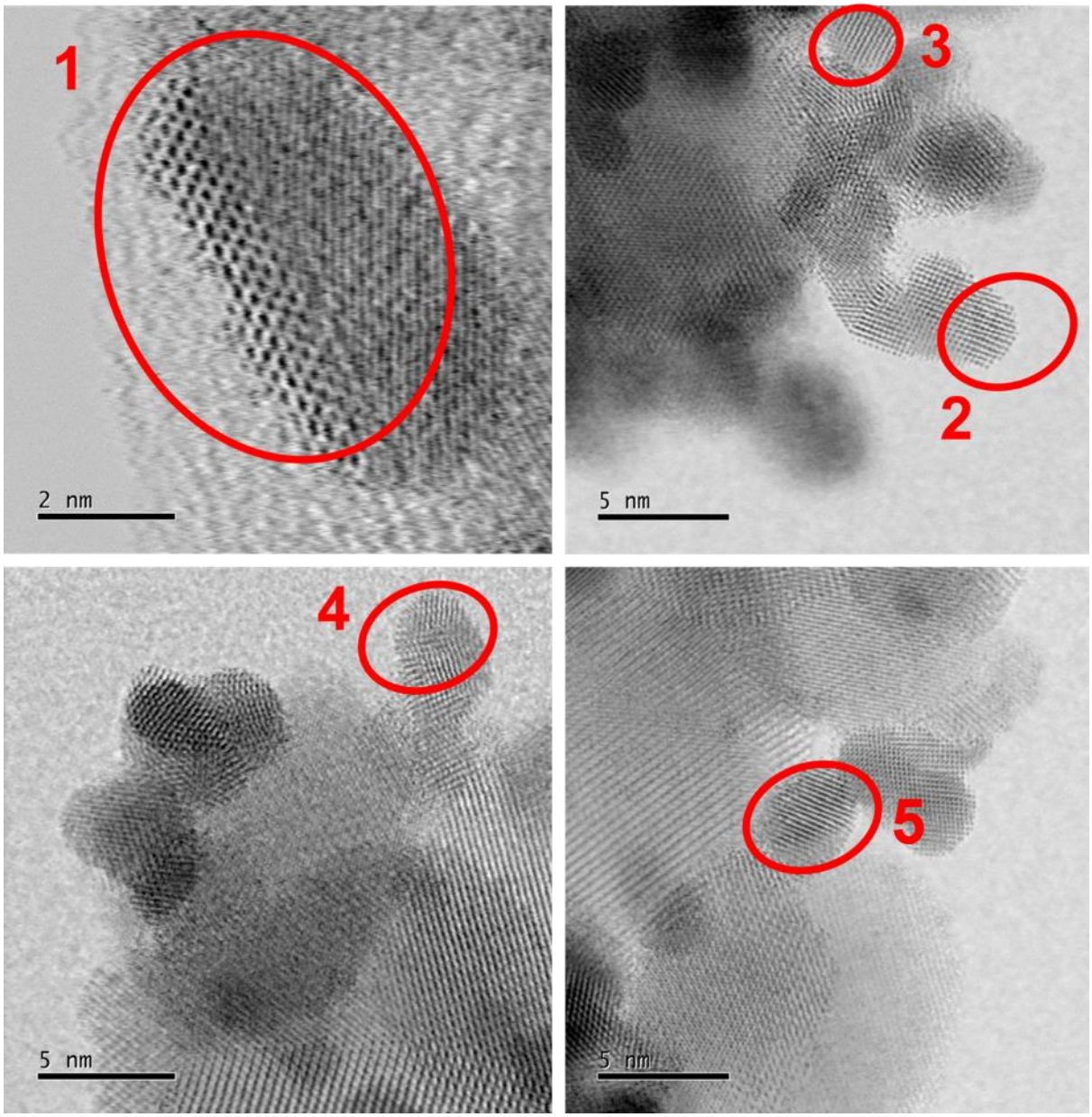


***Figure B-2:*** *HR-STEM images used for determination of lattice spacings in OMCD Ar-320°C $IrO_x$ particles.*

## B.3 POST-CHARACTERISATION HR-STEM IMAGES OF OMCD $IrO_X$/ATO

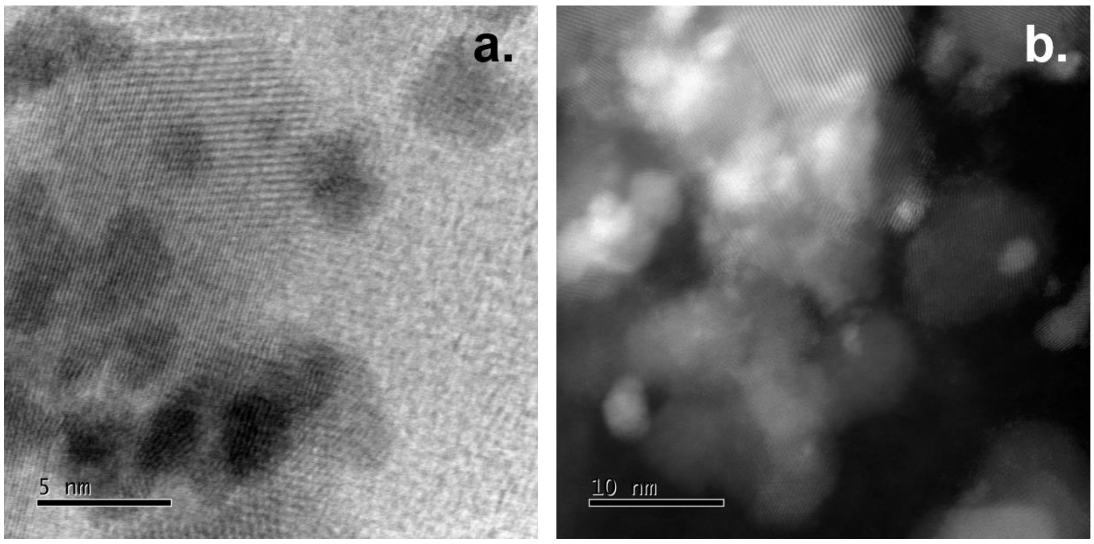


***Figure B-3:*** *HR-STEM images of OMD $IrO_x$/ATO after electrochemical characterisation.*

# Appendix C: Determination of Geometric $IrO_x$ Surface Area

## C.1 DENSITY OF Ir IN $IrO_2$

$$\rho(IrO_2) = 11.66\ g\ cm^{-3} = 11.66\ \times 10^{-21}\ g\ nm^{-3}$$

$$\rho(Ir\ in\ IrO_2) = \frac{Molar\ mass\ (Ir)}{Molar\ mass\ (IrO_2)} \times \rho(IrO_2)$$

$$= \left(\frac{192\ g\ mol^{-1}}{224\ g\ mol^{-1}}\right) \times\ 11.66\ \times 10^{-21}\ g\ nm^{-3} = 9.99\ \times 10^{-21}\ g\ nm^{-3}$$

## C.2 CALCULATION OF MASS-SPECIFIC SURFACE AREA USING $IrO_x$ PARTICLE DIAMETERS MEASURED USING HR-STEM

- Each equivalent particle diameter (d) that was measured by HR-STEM was converted into a surface area assuming spherical particle shape and the formula below:

$$Particle\ Surface\ Area\ (nm^2) = 4\pi\left(\frac{d}{2}\right)^2$$

- Each equivalent particle diameter (d) that was measured by HR-STEM was converted into a volume assuming spherical particle shape and the formula below:

$$Particle\ Volume\ (nm^3) = \frac{4}{3}\pi\left(\frac{d}{2}\right)^3$$

- Each particle volume was converted into a particle mass using the formula below:

$$Particle\ Mass\ (g) = \rho(Ir\ in\ IrO_2)\ \times Particle\ Volume$$

- The specific surface area of each catalyst excluding the surface area of the ATO support was calculated by the formula below:

$$Specific\ Surface\ Area\ \left(nm^2 {g_{Ir}}^{-1}\right) = \frac{\sum_{i=1}^{n} Particle\ Surface\ Area}{\sum_{i=1}^{n} Particle\ Mass}$$

- The resulting specific surface area was then converted to $m^2_{IrOx}\ g^{-1}_{Ir}$

## C.3 CALCULATED SPECIFIC-SURFACE AREAS FOR CATALYSTS $O_2$-320°C and Ar-320°C

***Table C-1:*** *Calculated specific surface area for catalysts $O_2$-320°C and Ar-320°C.*

| **Catalyst** | **Calculated Specific Surface Area / $m^2_{IrOx}\ g^{-1}_{Ir}$** |
|---|---|
| $O_2$-320°C | 217 |
| Ar-320°C | 146 |